Geophys. J. Int. (2009) **179,** 1113–1132 doi: 10.1111/j.1365-246X.2009.04329.x

Analysis of ambient noise energy distribution and phase velocity bias in ambient noise tomography, with application to SE Tibet

Huajian Yao and Robert D. van der Hilst

Department of Earth, Atmospheric, and Planetary Sciences, Massachusetts Institute of Technology, MA, USA. E-mail: hjyao@mit.edu

Accepted 2009 July 7. Received 2009 July 3; in original form 2009 February 13

SUMMARY

Green's functions (GFs) of surface wave propagation between two receivers can be estimated from the cross-correlation of ambient noise under the assumption of diffuse wavefields or energy equipartitioning. Interferometric GF reconstruction is generally incomplete, however, because the distribution of noise sources is neither isotropic nor stationary and the wavefields considered in the cross-correlation are generally non-diffuse. Furthermore, medium complexity can affect the empirical Green's function (EGF) from the cross-correlation if noise sources are all far away (i.e. approximately plane-wave sources), which makes the problem non-linear. We analyse the effect of uneven ambient noise distribution and medium heterogeneity and azimuthal anisotropy on phase velocities measured from EGFs with an asymptotic plane wave (far-field) approximation (which underlies most constructions of phase velocity maps). Phase velocity bias due to uneven noise distribution can be determined (and corrected) if the noise energy distribution and the velocity model are known. We estimate the (normalized) azimuthal distribution of ambient noise energy directly from the cross-correlation functions obtained through ambient noise interferometry. The (smaller, second order) bias due to non-linearity can be reduced iteratively, for instance by using the tomographic model that results from the inversion of uncorrected data. We illustrate our method for noise energy estimation, phase velocity bias suppression, and ambient noise tomography (including azimuthal anisotropy) with data from a seismic array (26 stations) in SE Tibet. We show that the phase velocity bias due to uneven noise energy distribution (and medium complexity) in SE Tibet has a small effect (<1 per cent) on the isotropic part phase velocities (for $T = 10$–30 s) and the azimuthal anisotropy obtained before and after bias correction shows very similar pattern and magnitude.

Key words: Interferometry; Surface waves and free oscillations; Seismic anisotropy; Seismic tomography; Crustal structure.

1 INTRODUCTION

Traditional surface wave tomography, based on ballistic source–receiver propagation, has produced important constraints on the long wavelength structure of Earth's upper mantle, both on global and regional scale. With this approach to (linearized) tomographic velocity analysis, however, the (uneven) source–receiver distribution controls (and restricts) the geographical regions that can be studied at high-resolution, and scattering from local heterogeneity and topography along the long wave paths can prevent accurate inversion for shallow structures, such as in Earth's crust. Instead of relying on source–receiver wave propagation, theoretical, experimental, and observational studies in ultrasonics, acoustics, and seismology have shown that the Green's function (GF) for wave propagation between two receivers can be recovered from cross-correlation of ambient wavefields (e.g. Lobkis & Weaver 2001; Campillo & Paul 2003; Malcolm *et al.* 2004; Shapiro & Campillo 2004; Snieder 2004; Wapenaar 2004; Weaver & Lobkis 2004; Roux *et al.* 2005; Nakahara 2006; Wapenaar *et al.* 2006). Indeed, surface wave array tomography from ambient noise interferometry (e.g. Sabra *et al.* 2005; Shapiro *et al.* 2005; Kang & Shin 2006; Yao *et al.* 2006, 2008; Lin *et al.* 2007, 2008; Moschetti *et al.* 2007; Yang *et al.* 2007, 2008; Liang & Langston 2008; Zheng *et al.* 2008) has greatly improved our ability to resolve the shallow crust structure by extracting short periods group or phase velocity dispersion measurements from the recovered empirical Green's function (EGF).

Inferring the (empirical) GF from time domain cross-correlations is conceptually simple, but in general the EGF differs from the exact GF and this (unknown) difference is becoming more important when applications are pushed to higher accuracy or medium complexity (e.g. anisotropy). Correct reconstruction of the GF requires diffuse fields (Lobkis & Weaver 2001), isotropic noise source distribution (e.g. Snieder 2004; Roux *et al.* 2005) or isotropic incidence of wavefields (Nakahara 2006), in the dimensions relevant for application at hand (e.g. 2-D for surface wave GFs). Recent surface wave studies show that the actual distribution of ambient noise energy is, in general, neither isotropic nor stationary but reveals directional and temporal variations (Stehly *et al.* 2006; Yang & Ritzwoller 2008a; Yao *et al.* 2009). As a consequence, the EGF is generally an incomplete reconstruction of the true GF, which can be manifest, for instance, in a lack of reciprocity of the EGFs between two receivers (e.g. Yao *et al.* 2006).

The uneven distribution of noise sources can produce a bias in the surface wave group or phase velocities measured from the EGFs. Furthermore, if the predominant noise sources are all far away so that wave energy propagating across the receiver array can be approximated as plane waves, the (unknown) medium heterogeneity can also produce traveltime bias from the EGFs even for an isotropic distribution of noise energy (e.g. Tsai 2009). However, in case of spatially homogeneous distribution of noise sources or diffuse wavefields, we would expect accurate traveltime measurements from the EGFs regardless of any medium complexity. Comparisons of phase velocities from ambient noise interferometry and traditional two-station analysis (Yao *et al.* 2008) and of phase velocity maps from ambient noise tomography and teleseismic surface wave tomography (Yang & Ritzwoller 2008b) as well as numerical simulations for certain types of noise distribution (Lin *et al.* 2008; Yang & Ritzwoller 2008a) indicate that the bias is, indeed, small for the types of study done so far. It appears that the use of long time windows for cross-correlation (e.g. 1 yr) and temporal and spectral normalization before cross-correlation, for example, one-bit (Shapiro & Campillo 2004) or running-absolute-mean normalization and whitening (Bensen *et al.* 2007), are efficient in making the distribution of ambient noise sources more isotropic. Any remaining non-isotropic component of the ambient noise distribution will, however, result in an azimuth-dependence of bias of the phase or group velocity measurements from EGFs, and these discrepancies may be significant for high-resolution studies or for determination of azimuthal and radial anisotropy.

de Hoop & Solna (2008) present a multiscale analysis of GFs estimated from 'field–field' correlations in a random medium. Closer to the problem of interest here, Tsai (2009) corrects phase or group velocity bias using estimated traveltimes between two stations for given distribution of (ambient noise) source intensity. With synthetic data he shows that both the azimuthally uneven distribution of source intensity and the heterogeneity of the medium can produce bias in surface wave dispersion measurements. Stehly *et al.* (2006) and Yang & Ritzwoller (2008a) investigated the azimuth-dependence of ambient noise energy using a back projection method. Brzak *et al.* (2008) introduced a migration approach to estimate the noise energy distribution from the cross-correlation functions. Harmon *et al.* (2008) and Yao *et al.* (2009) used a plane-wave beamforming analysis to estimate the ambient noise energy distribution. However, all these approaches still did not provide a quantitative measure of ambient noise energy distribution directly related to the recovery of surface wave GF from the cross-correlation, which is needed to actually correct the bias.

We describe here an approach to estimate the energy distribution of ambient noise and to correct the phase velocity bias for ambient noise surface wave array tomography. We illustrate the problems—and solutions—with data from a seismograph array in SW China (Yao *et al.* 2006, 2008). The accuracy of GF reconstruction from ambient noise interferometry depends on (i) the azimuthal distribution of noise energy (even versus uneven), (ii) the type of medium (homogeneous versus heterogeneous; isotropic versus anisotropic) in case of plane-wave source distribution and (iii) the scales in the data (frequency) and medium (structural length scales). It is impractical to explore all possible cases but the examples shown here give insight in the type and magnitude of the problem and the promise of the solution. In Section 2, we analyse cross-correlations (and associated EGFs) and present our approach to bias estimation through (asymptotic) plane-wave modelling. Section 3 investigates phase velocity bias through stationary phase and Fresnel zone arguments for different types of noise distribution and medium. Section 4 presents a damped least-squares inversion that can be used to estimate the azimuthal variations of ambient noise energy from the (given) correlation functions. In Section 5, we apply the proposed method for noise energy estimation and phase velocity bias correction to array data in SE Tibet with an iterative approach. Finally, we discuss the importance of analysis of phase velocity bias and noise energy estimation for isotropic and anisotropic ambient noise tomography.

2 PLANE-WAVE MODELLING AND INTERFEROMETRY

We investigate the surface wave part from ambient noise interferometry and ignore other types of waves generated by the noise sources. If the aperture of an array is small compared to the distance to the main noise sources—many ambient noise tomography studies concern arrays a few hundred kilometres across (e.g. SE Tibet, by Yao *et al.* 2006, 2008; New Zealand, by Lin *et al.* 2007; South Korea, by Cho *et al.* 2007)—we can approximate the energy from ambient noise sources as plane waves, for instance, in a theoretical framework by Nakahara (2006) and Tsai (2009). This plane wave approximation is also widely adopted in regional surface wave array analysis (e.g. Yang & Ritzwoller 2008b). We represent the noise energy as $E_P(\omega, \theta)$, with ω the angular frequency and θ the azimuth angle of the incoming plane wave passing across the array. Local scattering due to heterogeneity of the medium within or close to the array is not considered but their contribution is probably small compared to that from direct waves (like ocean- or earthquake-generated surface waves) (Yao *et al.* 2009). Note that $E_P(\omega, \theta)$ represents the total energy of the plane waves with azimuth θ propagating across the array, which may have contributions from many ambient noise sources. We use 'plane wave energy' $E_P(\omega, \theta)$ and 'ambient noise energy' as synonymous throughout this paper. For simplicity we assume straight rays but there is no obstruction for expanding the method to include ray bending or finite frequency sensitivities.

We consider seismograph stations at locations A and B in a 2-D elastic medium (Fig. 1). The incoming plane wave with azimuth angle θ and energy $E_P(\omega, \theta)$ is assumed to be recorded at both stations with equal amplitude—one-bit cross-correlation (e.g. Yao *et al.* 2006) or normalized cross-correlation (Bensen *et al.* 2007) removes the effect of geometrical spreading and attenuation. The phase traveltime difference δt (or phase delay $\delta\phi = \omega\delta t$) of the plane wave between the two stations will result in a peak in the cross-correlation function. The summation of cross-correlation functions from all plane waves with azimuth angle from 0 to 2π produces the final cross-correlation function,

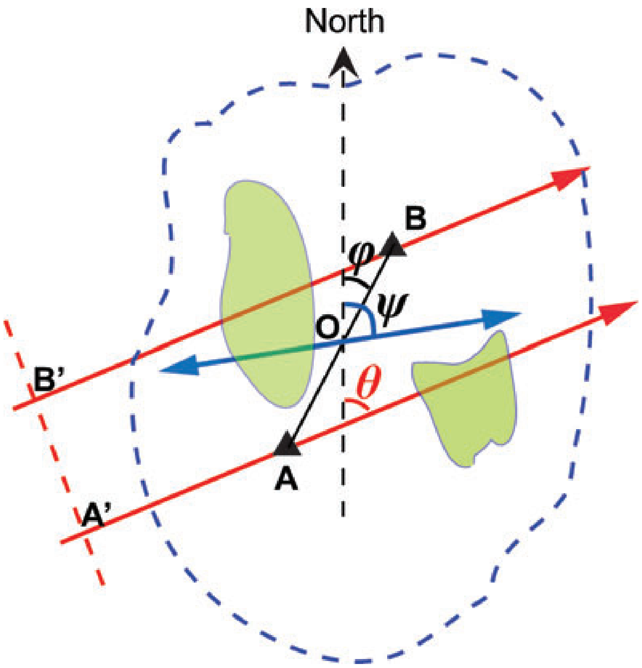

Figure 1. Geometry of the plane-wave modelling. The incoming plane wave with azimuth angle θ is shown as the red lines with arrow. Red dashed line shows the wave front of the plane wave, which is perpendicular to the ray paths. The two stations are located at A and B, shown as the black triangles, with the central point at O and azimuth angle φ (from A to B). The green patches are the regions with velocity anomalies. The fast direction with the azimuth angle ψ of the azimuthal anisotropy at point O is shown as the blue bar with arrows at both ends.

$C_{AB}(\omega, t)$, between stations A and B

$$C_{\mathrm{AB}}(\omega, t) = \int_0^{2\pi} E_P(\omega, \theta) \cos\left[\omega(t - \delta t)\right] H(t, \delta t) \mathrm{d}\theta, \tag{1}$$

where t is time and $H(t, \delta t)$ a time domain taper for the cross-correlation function $E_P(\omega, \theta)\cos[\omega(t - \delta t)]$, which is infinite in time (blue sinusoid trace in Fig. 2a). We use for $H(t, \delta t)$ a simple cosine taper function with peak centred at δt (dashed trace, Fig. 2a)

$$H(t, \delta t) = \begin{cases} 0.5\left\{1 + \cos[2\pi(t - \delta t)/T^*]\right\} & t \in [\delta t - T^*/2, \delta t + T^*/2] \\ 0 & \text{elsewhere} \end{cases}, \tag{2}$$

where T^* is the (time) width of $H(t, \delta t)$. Here we choose $T^* = 5T$, with $T = 2\pi/\omega$ the period of the sinusoid wave. The integrant in eq. (1) denotes the individual cross-correlation function of the incoming plane wave with azimuth angle θ.

For homogeneous and isotropic medium with phase velocity c, the phase delay of the plane wave (with azimuthal angle θ) between stations A and B (Fig. 1) is

$$\delta\phi = k\Delta_{\mathrm{AB}} \cos(\theta - \varphi) = \omega\Delta_{\mathrm{AB}} \cos(\theta - \varphi)\big/c, \tag{3}$$

where $k = \omega/c$ is the wavenumber, Δ_{AB} is the interstation distance and φ is the azimuth angle from station A to station B measured from north.

For a homogeneous but azimuthally anisotropic medium, Rayleigh wave phase velocity c can be approximated by $c = c_0\{1 + A_c \cos 2(\theta - \psi)\}$(Smith & Dahlen 1973), where c_0 is the transversely isotropic part of the phase velocity, A_c is the amplitude of the azimuthal anisotropy and ψ is the fast direction of the medium. For general heterogeneous and azimuthally anisotropic medium (Fig. 1), the phase delay $\delta\phi$ between two stations is

$$\delta\phi = \int_{\mathrm{B}'}^{\mathrm{B}} \frac{\omega}{c(\omega, \mathbf{x})} \mathrm{d}l - \int_{\mathrm{A}'}^{\mathrm{A}} \frac{\omega}{c(\omega, \mathbf{x})} \mathrm{d}l, \tag{4}$$

where $\mathbf{x}$ is the spatial coordinate and the integration is along the ray path B′B and A′A as shown in Fig. 1.

The time derivative of the ambient noise cross-correlation function $C_{\mathrm{AB}}(\omega, t)$ yields the EGFs $\tilde{G}_{\mathrm{AB}}(\omega, t)$ and $\tilde{G}_{\mathrm{BA}}(\omega, t)$

$$\begin{aligned} \frac{\mathrm{d}C_{\mathrm{AB}}(\omega, t)}{\mathrm{d}t} &= -\tilde{G}_{\mathrm{AB}}(\omega, t) + \tilde{G}_{\mathrm{BA}}(\omega, -t) \\ \tilde{G}_{\mathrm{AB}}(\omega, t) &= -\frac{\mathrm{d}C_{\mathrm{AB}}(\omega, t)}{\mathrm{d}t} \quad t \geq 0 \\ \tilde{G}_{\mathrm{BA}}(\omega, t) &= -\frac{\mathrm{d}C_{\mathrm{AB}}(\omega, -t)}{\mathrm{d}t} \quad t \geq 0. \end{aligned} \tag{5}$$

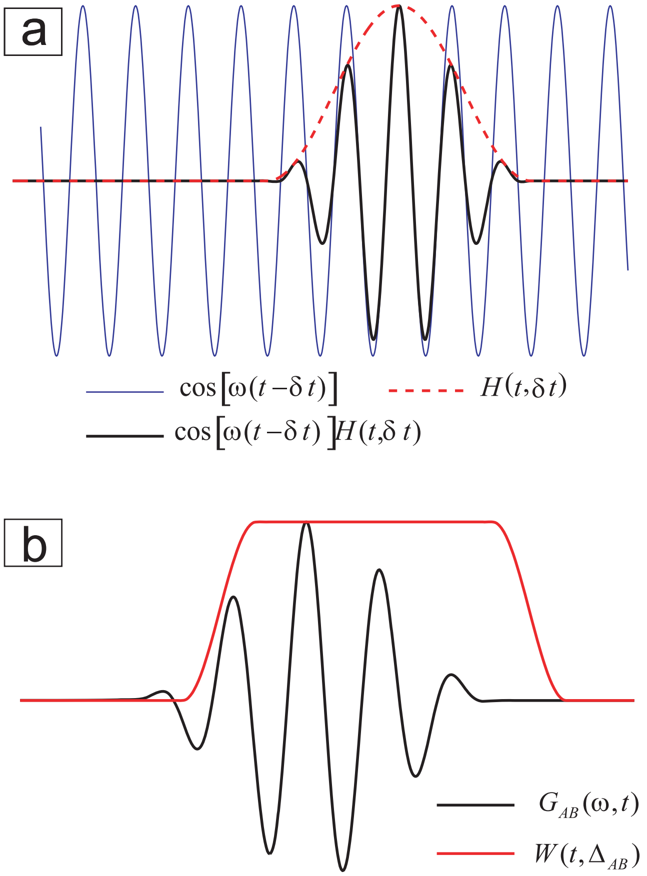

Figure 2. (a) Taper function $H(t, \delta t)$, shown as the red dashed trace, as given by eq. (2). The blue trace show the single sinusoid cross-correlation function $\cos[\omega(t - \delta t)]$ of incoming plane wave and the black trace gives the product of $H(t, \delta t)$ and $\cos[\omega(t - \delta t)]$. (b) Surface wave window function $W(t, \Delta_{\mathrm{AB}})$, shown as the red trace, as given by eq. (7). The black trace shows the theoretical Green's function given by eq. (6).

Under the assumption of isotropic wavefields or homogeneous distribution of noise sources, theoretical studies (e.g. Weaver & Lobkis 2004; Snieder 2004; Roux *et al.* 2005) have demonstrated that the EGF $\tilde{G}_{\mathrm{AB}}(\omega, t)$ [or $\tilde{G}_{\mathrm{BA}}(\omega, t)$] is equivalent to the real GF $G_{\mathrm{AB}}(\omega, t)$ [or $G_{\mathrm{BA}}(\omega, t)$], that is the GF that would have been recorded at station at B for a point source at A (or GF recorded at station A for a point source at B), except for a frequency-dependent amplitude correction. The phase of EGF is the same as that of GF.

In the far field (loosely, several wavelengths apart) the time-domain windowed GF for the surface wave fundamental mode centred at frequency ω can be approximated by (e.g. Dahlen & Tromp 1998)

$$G_{\mathrm{AB}}(\omega, t) = A\cos(\bar{k}_{\mathrm{AB}}\Delta_{\mathrm{AB}} - \omega t + \pi/4)H(t, t_{\mathrm{AB}}), \qquad (6)$$

where A is the amplitude of surface wave GF, $\bar{k}_{\mathrm{AB}} = \frac{1}{\Delta_{\mathrm{AB}}}\int_{\mathrm{A}}^{\mathrm{B}} k(\omega, \mathbf{x})\mathrm{d}l$ the path average wavenumber between A and B, $H(t, t_{\mathrm{AB}})$ the taper defined as eq. (2), and $t_{\mathrm{AB}} = (\bar{k}_{\mathrm{AB}}\Delta_{\mathrm{AB}} + \pi/4)/\omega$ the phase traveltime of surface wave fundamental mode at frequency ω. In the context of phase velocity maps, which is an asymptotic concept, we assume great circle propagation of surface waves between A and B.

In order to compare the $\tilde{G}_{\mathrm{AB}}(\omega, t)$ and $G_{\mathrm{AB}}(\omega, t)$ in the same time window, we define a surface wave window function (black trace, Fig. 2b)

$$W(t, \Delta_{\mathrm{AB}}) = \begin{cases} 1 & t \in [t_L, t_U] = [\Delta_{\mathrm{AB}}/v_{\max}, \Delta_{\mathrm{AB}}/v_{\min}] \\ 0.5\left\{1 + \cos[\pi(t - t_U)/T]\right\} & t \in (t_U, t_U + T] \\ 0.5\left\{1 + \cos[\pi(t_L - t)/T]\right\} & t \in [t_L - T, t_L) \\ 0 & \text{elsewhere} \end{cases}, \qquad (7)$$

where $v_{\min}$ and $v_{\max}$ are the minimum and the maximum group velocities to define the main surface wave window, respectively. $W(t, \Delta_{\mathrm{AB}})$ can be frequency-dependent. For typical regional ambient noise surface wave tomography in the period band 10–50 s, $v_{\min} \approx 2$ km s^{-1} and $v_{\max} \approx 5$ km s^{-1}. For very short periods (e.g. several seconds), the group velocities that define the surface wave window will depend on the wave speeds at shallow depth (e.g. top few kilometres).

Inside $W(t, \Delta_{\mathrm{AB}})$ we measure the phase difference ($\delta\phi_{\mathrm{AB}}$) between the EGF, $\tilde{G}_{\mathrm{AB}}(\omega, t)$ and the theoretical GF, $G_{\mathrm{AB}}(\omega, t)$, at frequency ω

$$\delta\phi_{\mathrm{AB}}(\omega) = \Theta[\tilde{G}_{\mathrm{AB}}(\omega, t)W(t, \Delta_{AB})] - \Theta[G_{\mathrm{AB}}(\omega, t)W(t, \Delta_{AB})], \qquad (8)$$

where Θ is the operator to obtain the phase angle of a trace at frequency ω (for example, one can take the Fourier transform of the trace and calculate the phase from the real and imaginary part of spectrum at frequency ω). The traveltime difference between EGF and GF is then given by $\delta t_{\mathrm{AB}} = \delta\phi_{\mathrm{AB}}(\omega)/\omega$. If $\delta\phi_{\mathrm{AB}} > 0$, the surface wave EGF has a phase shift away from zero time with respect to the theoretical surface wave GF; in other words, the phase traveltime of the empirical surface wave recovered from noise correlation is larger than that of theoretical surface wave. In this case the apparent phase velocity obtained from the EGF is slower than that from the theoretical GF. For $\delta\phi_{\mathrm{AB}}$ or δt_{AB} less than zero, we would expect a higher phase velocity from the EGF than that from the theoretical GF. The relative phase velocity bias (μ) between the EGF and GF can then be expressed as

$$\mu = \frac{\tilde{c}_{\mathrm{AB}} - c_{\mathrm{AB}}}{c_{\mathrm{AB}}} \approx -\frac{\delta t_{\mathrm{AB}}}{t_{\mathrm{AB}}} = -\frac{\delta\phi_{\mathrm{AB}}(\omega)}{\omega t_{\mathrm{AB}}}, \tag{9}$$

where $\tilde{c}_{\mathrm{AB}}$ and c_{AB} are the surface wave phase velocities of the EGF and GF, respectively.

3 AZIMUTH DEPENDENT PHASE VELOCITY BIAS

As shown above, with plane-wave modelling we can estimate the bias, that is, the relative difference between (fundamental mode) surface wave phase velocities measured from EGF and GF for a known ambient noise energy distribution $E_P(\omega, \theta)$ and medium. We illustrate this with an isotropic and a realistic azimuth dependent ambient noise energy distribution and with simple models for structural heterogeneity and anisotropy. The geometry of the experiments is given in Fig. 1, with φ the azimuth from A to B measured from north. Unless otherwise mentioned, the period of the plane wave $T = 30$ s, the distance between the stations $l_{\mathrm{AB}} = 480$ km with central point fixed at O, and the background phase velocity $c_0 = 4$ km s^{-1}. In all examples we consider—for eq. (1)—incoming plane waves with θ from 0–360° in intervals $\mathrm{d}\theta = 0.5°$.

3.1 Homogeneous and isotropic medium

3.1.1 Isotropic energy distribution

For an isotropic distribution of ambient noise energy, that is, $\partial E_P(\omega,\theta)/\partial\theta = 0$, and station pair AB in S-N direction (that is, $\varphi = 0°$), Fig. 3(a) shows cross-correlation functions for plane waves arriving from 0° to 360°. The maximum plane wave traveltime difference between A and B is $\delta t_{\max} = 120$ s for a northward propagating plane wave ($\theta = 0°$ or 360°), and $\delta t_{\min} = -120$ s for a southward propagating plane wave ($\theta = 180°$). For waves perpendicular to A–B ($\theta = 90°$ or 270°), $\delta t = 0$ s. Following (1), the sum of individual cross-correlations gives the cross-correlation function $C_{\mathrm{AB}}(\omega, t)$ for stations A and B (blue line, Fig. 3b). The time derivative of $C_{\mathrm{AB}}(\omega, t)$ then yields the EGF (red dashed line, Fig. 3b).

The appearance of two arrivals in $C_{\mathrm{AB}}(\omega, t)$ (and EGF) can be understood both with stationary phase (e.g. Snieder 2004) and Fresnel zone analysis. The individual cross-correlation functions from plane waves propagating with the azimuth near the two-station line, that is, small $|\theta - \varphi|$, interfere (stack) constructively (near $\delta t = \pm 120$ s), whereas waves with larger $|\theta - \varphi|$ interfere destructively and do not contribute to $C_{\mathrm{AB}}(\omega, t)$. With λ the wavelength, constructive interference occurs if

$$|\Delta_{\mathrm{AB}} \cos(\theta - \varphi) - \Delta_{\mathrm{AB}}| < \lambda/2, \tag{10}$$

which defines the first Fresnel for a homogeneous and isotropic medium, or

$$|\Delta\phi(\theta)| = \left| \left\{ \int_{\mathrm{B}'}^{\mathrm{B}} \frac{\omega}{c(\omega, \mathbf{x})} \mathrm{d}l(\theta) - \int_{\mathrm{A}'}^{\mathrm{A}} \frac{\omega}{c(\omega, \mathbf{x})} \mathrm{d}l(\theta) \right\} - \int_{\mathrm{A}}^{\mathrm{B}} \frac{\omega}{c(\omega, \mathbf{x})} \mathrm{d}l(\varphi) \right| < \pi \tag{11}$$

for a general heterogeneous medium. In (11), $\Delta\phi(\theta)$ is the phase difference between the individual cross-correlation function from the incoming plane wave with azimuth θ and ray path $l(\theta)$ and the individual cross-correlation function from the plane wave propagating along the interstation ray path $l(\varphi)$ from A to B. Plane waves within the first Fresnel zone, that is, with θ satisfying (10) or (11), contribute most to the construction of the GF. Plane waves outside the first Fresnel zone either cancel out through destructive interference (as in the example shown) or give spurious arrivals if destructive interference is incomplete owing to, for instance, uneven distribution of ambient noise energy. For the parameters given, the first Fresnel zone consists of two parts: $0° \le \theta < 28.9°$ and $331.1° \le \theta < 360°$ (yellow boxes, Fig. 3a) for the construction of $G_{\mathrm{AB}}(\omega, t)$ and $|\theta–180°| < 28.9°$ (red box, Fig. 3a) for the construction of $G_{\mathrm{BA}}(\omega, t)$. Here, the EGF (red dashed line, Fig. 3b) is nearly identical to the real GF (black line), with zero phase shift for both the causal (positive-time) and acausal (negative-time) part, as expected from theory (e.g. Weaver & Lobkis 2004; Roux *et al.* 2005; Nakahara 2006).

3.1.2 Uneven energy distribution

For uneven distribution of plane-wave sources we consider two cases. In the first, ambient noise generated plane waves only propagate along the direction of the two-station path, that is, $E_P(\omega, \theta) > 0$ for $\theta = \varphi$ or $\theta = \pi + \varphi$ and $E_P(\omega, \theta) = 0$ elsewhere. The cross-correlation function obtained (blue line, Fig. 3c) is the same as in traditional two-station analysis (e.g. Yao *et al.* 2006) but has a $\pi/4$ phase advance compared to the GF (black lines, Figs 3b and c). Since the EGF (red dashed lines, Fig. 3c) is $\pi/2$ phase delayed (away from zero time) with respect to $C_{AB}(\omega, t)$, as expected from the negative time derivative, there is a $\pi/4$ phase shift between EGF and GF.

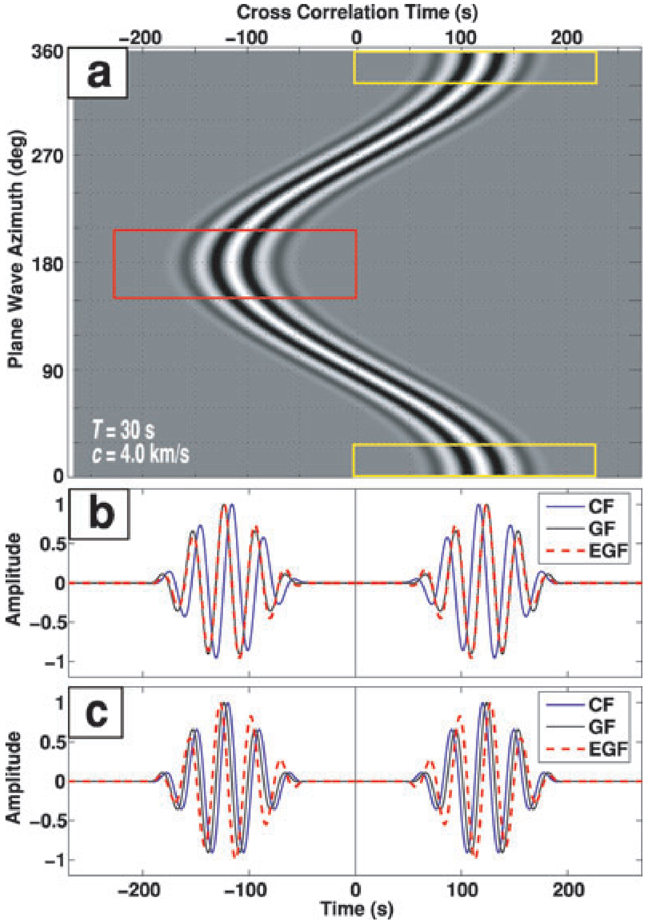

Figure 3. Illustration of the construction of Green's function from 30 s period plane wave interferometry in a homogeneous and isotropic medium with phase velocity $c = 4$ km s^{-1} at period 30 s. (a) Cross-correlagram for a south-north station pair apart from 480 km with isotropic plane wave energy distribution. Each horizontal line in the cross-correlagram gives the individual cross-correlation function, given by the integrand of eq. (1). The white colour represents the positive values while the black colour shows for negative values. The red box shows the first Fresnel zone of plane wave interferometry, given by eq. (10), for the construction of the anticausal part Green's function, while the yellow boxes shows that for the causal part Green's function. (b) Comparison of the cross-correlation function (CF), empirical Green's function (EGF), and the theoretical Green's function (GF) for isotropic noise energy distribution with cross-correlagram shown in (a). CF (blue trace) is the stack of all individual cross-correlation functions, that is, vertical directional stack of the cross-correlagram in (a). EGF (red dashed trace) has $\pi/2$ phase shift to CF but is almost identical to the theoretical GF (black trace). (c) Comparison of the CF, EGF and GF when plane wave energy is 1 only at azimuth angle $\theta = 0^\circ$ and 180° but zero elsewhere. In this case, the EGF has $\pi/4$ phase shift away from zero time compared to the GF.

For the second case we consider a more realistic, azimuth-dependent (normalized) ambient noise energy distribution (black curve, Fig. 4a), inferred from our study in SW China (Yao *et al.* 2009). The azimuth dependence of the (normalized) amplitude of the cross-correlation functions, $C_{\mathrm{AB}}(\omega, t)$, blue curve in Fig. 4(a), differs from that of the ambient noise energy (black curve), indicating that $C_{\mathrm{AB}}(\omega, t)$ cannot be used as a proxy for $E_P(\omega, \theta)$. As a consequence, the phase velocity bias between EGF and GF (blue line, Fig. 4b) depends on azimuth: that is, $\mu = \mu(\theta)$. The largest phase velocity biases occur where $E_P(\omega, \theta)$ changes most rapidly with azimuth (for instance, between 0° and 90° and between 180° and 270°, Fig. 4a), with up to 3 per cent bias for some station pairs (e.g. $\varphi \sim 20^\circ$ or 70°). For relatively smooth azimuthal variation of ambient noise energy (e.g. 90°–160° or 270°–315°) the phase velocity bias is small (<1 per cent).

As discussed above, energy within the first Fresnel zone controls the recovery of the GF of the phase of interest. One would expect that the better the distribution of noise sources within the Fresnel zone the smaller the bias in phase velocity. Fig. 4(b) shows, however, that bias can vanish (e.g. at $\varphi \sim 32^\circ$ and 58°) even if the ambient noise energy distribution within the Fresnel zone is heterogeneous. In a homogeneous and isotropic medium, plane waves with azimuth $\theta = \varphi - \Delta\theta$ and $\theta = \varphi + \Delta\theta$ contribute equally to the recovery of $G_{\mathrm{AB}}(\omega, t)$ at station pair with angle φ, so that adequate distribution in half of the Fresnel zone is generally sufficient to prevent bias.

3.2 Homogeneous and azimuthally anisotropic medium

In the previous section we considered only the effect of uneven ambient noise energy distribution. Here we use similar experiments to assess the effect of noise energy distribution on phase velocity bias in the presence of azimuthal anisotropy. We recall that the GFs used here are

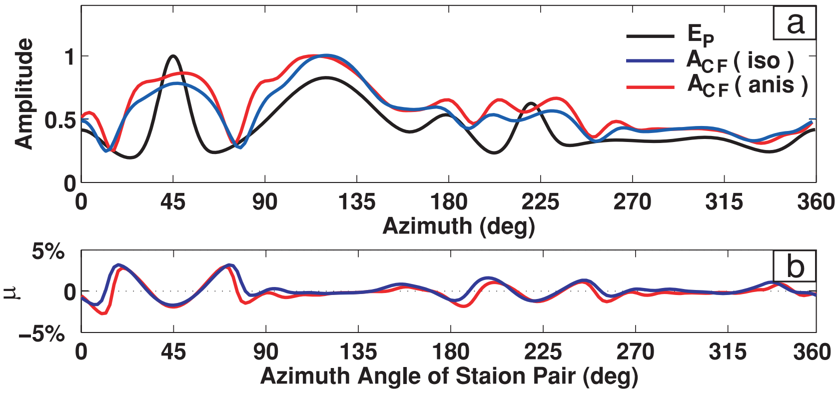

Figure 4. Bias of phase velocity measurements from plane wave interferometry in case of non-isotropic plane wave energy distribution in homogeneous medium with or without azimuthal anisotropy: (a) azimuthal distribution of ambient noise energy E_P (shown as the black curve) and normalized surface wave amplitudes A_{CF} of the cross-correlation functions (blue or red curve); and (b) relative phase velocity bias (μ) between the EGF and GF as given by eq. (9). The blue curve represents for the bias for a homogeneous and isotropic medium and the red curve for a homogeneous medium with 5 per cent azimuthal anisotropy with fast direction $\psi = 45^\circ$. The geometry of the station pair is described in Section 3.

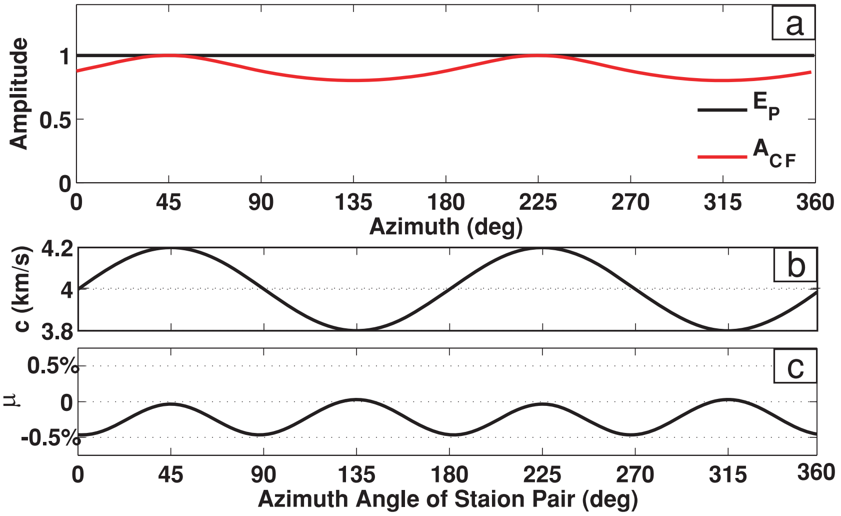

Figure 5. Relative phase velocity bias (μ) [black line in (c)] for an isotropic ambient noise energy distribution [black line in (a)] in a homogeneous medium with 5 per cent azimuthal anisotropy with fast direction $\psi = 45^\circ$. In (a) the red line shows the normalized surface wave amplitudes A_{CF} of the cross-correlation functions. In (b) the black line shows the interstation phase velocity with different azimuth angles.

evaluated with a ray theoretical approximation. In heterogeneous media the full wave GF may be different, but the (scale dependent) difference is expected to be small.

3.2.1 Isotropic energy distribution

Under the plane wave approximation, azimuthal anisotropy can cause phase shifts between EGF and GF, even for an isotropic energy distribution. The effect is small, however. For a homogeneous, 5 per cent azimuthally anisotropic medium (with fast axis at $\psi = 45^\circ$, along the NE–SW direction) the phase velocity bias $\mu(\theta)$ is generally less than 0.5 per cent (Fig. 5c). The bias vanishes for station pairs in the direction of zero phase velocity gradient (in the first Fresnel zone), for example, $\varphi = 45^\circ$, 135°, 225° and 315° (Figs 5b and c) and is largest for the station pairs with the largest velocity gradient with respect to azimuth, for example, $\varphi = 0^\circ$, 90°, 180° and 270° (Figs 5b and c).

3.2.2 Uneven energy distribution

To assess the effect of medium anisotropy on GF reconstruction and phase velocity bias in the presence of uneven energy distribution we use the same $E_P(\omega, \theta)$ as in Section 3.1.2 (black line, Fig. 4a). The variations with azimuth of (normalized) amplitude of the cross-correlations and bias μ (red lines in Figs 4a and b) are virtually the same as in the isotropic case (blue lines, Figs 4a and b), with large biases occurring near azimuths where ambient noise energy changes rapidly with respect to station pair azimuth φ. From tests like this we conclude that the

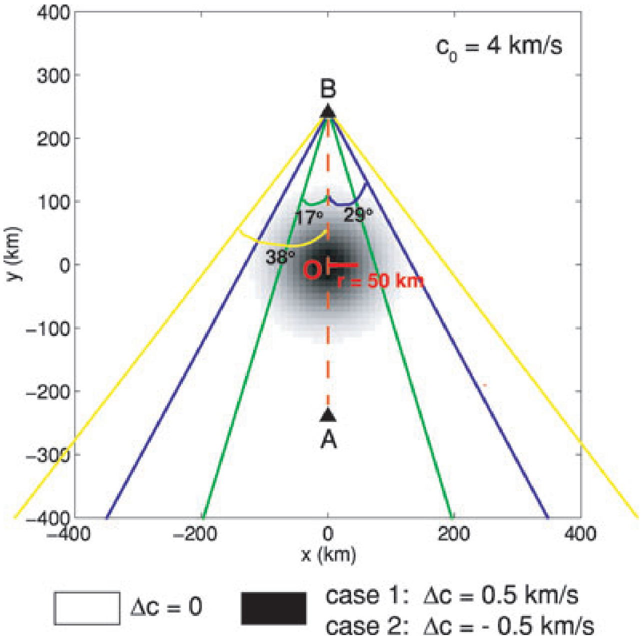

Figure 6. Geometry of plane wave interferometry for a heterogeneous and isotropic medium (Section 3.3.1) with isotropic ambient noise energy distribution. The velocity distribution is $c(x, y) = c_0 + \Delta c \cdot \exp\{-0.5(x^2 + y^2)/r^2\}$, with the background velocity $c_0 = 4$ km s^{-1} shown as the white region and the 2-D Gaussian shape anomaly centred at O(0, 0) shown as the black-shaded region with the characteristic horizontal scale r. The largest anomaly, $\Delta c = 0.5$ km s^{-1} for case 1 or $\Delta c = -0.5$ km s^{-1} for case 2, is shown with black. The two stations at A (0, −240) and B (0, 240) are shown as the black triangles. For an anomaly with the horizontal scale $r = 50$ km and $\Delta c = 0.5$ km s^{-1}, the half width of the first Fresnel zone for interferometry (see eq. (11)) with respect to the two-station path (from A to B) is about 17°, 29° and 38° for $T = 10$, 30 and 50 s, as bounded with the green, blue and yellow lines, respectively.

bias in phase velocity (from EGFs) due to (weak) azimuthal anisotropy is much smaller than that of uneven distribution of ambient noise energy.

3.3 Heterogeneous and anisotropic medium

Finally, we examine the effect of ambient noise energy distribution on phase velocity bias $\mu(\theta)$ in the presence of both azimuthal anisotropy and (2-D) medium heterogeneity.

3.3.1 Isotropic energy distribution

Much like azimuthal anisotropy (previous section), medium heterogeneity can bias phase velocities measured from EGFs even for an isotropic energy distribution due to the assumption of distant (plane-wave) sources. In a first experiment we consider a Gaussian anomaly—centred on O between A and B (Fig. 6)—expressed as $c(x,y) = c_0 + \Delta c \exp\{-0.5(x^2 + y^2)/r^2\}$, where $c_0 = 4.0$ km s^{-1} is the background wave speed, Δc (0.5 km s^{-1} for case 1 and −0.5 km s^{-1} for case 2) the magnitude of the anomaly, x and y spatial coordinates and r the characteristic length (in km) of the anomaly. Since the velocity distribution is rotationally symmetric the average phase velocity for any station pair azimuth φ will be equal; for the following calculation we take the station pair with $\varphi = 0°$ (Fig. 6).

To investigate the dependence of bias on spatial scale (of medium heterogeneity), we fix the period of incoming plane waves T at 30 s and let r increase from 2 to 150 km (Fig. 7a). For case 1, that is $\Delta c = 0.5$ km s^{-1}, the resulting phase traveltime difference δt_{AB} between EGF and the theoretical GF is close to zero for r less than several kilometres or larger than ∼100 km, but δt_{AB} will be as much as 1 s for r around 35 km. The latter would correspond to a phase velocity measured from EGF that is ∼1 per cent slower than from GF. In case 1, $\delta t_{\mathrm{AB}} \geq 0$ for all r, which implies that phase velocities estimated from EGFs are always less than the theoretical phase velocities. Likewise, for case 2($\Delta c = -0.5$ km s^{-1}), $\delta t_{\mathrm{AB}} \leq 0$ for any r, indicating that the phase velocity will be overestimated.

This can, again, be understood with a simple Fresnel zone analysis. For the geometry given (Fig. 6), the average velocity will (for case 1) be largest between the two stations. Plane waves propagating off the two-station path but within the first Fresnel zone (and thus relevant for the construction of the EGF) will sense lower average velocities and thus render a larger travel difference δt_{AB} than in a homogeneous, isotropic medium, with phase velocity the average interstation velocity. This results in a lower phase velocity, that is, a phase velocity bias $\mu < 0$. Similarly, $\Delta c < 0$ leads to $\mu > 0$. For small r the average phase velocity between A and B is close to c_0 and for very large scale anomalies (here, $r > 100$ km) plane waves within the first Fresnel zone all propagate with speeds similar to the interstation average. For both cases, δt_{AB} (within the first Fresnel zone) will be very similar to that in a homogeneous and isotropic medium, and therefore the final phase velocity estimation from the EGF will be very close to that from the theoretical GF, that is, $\mu \sim 0$.

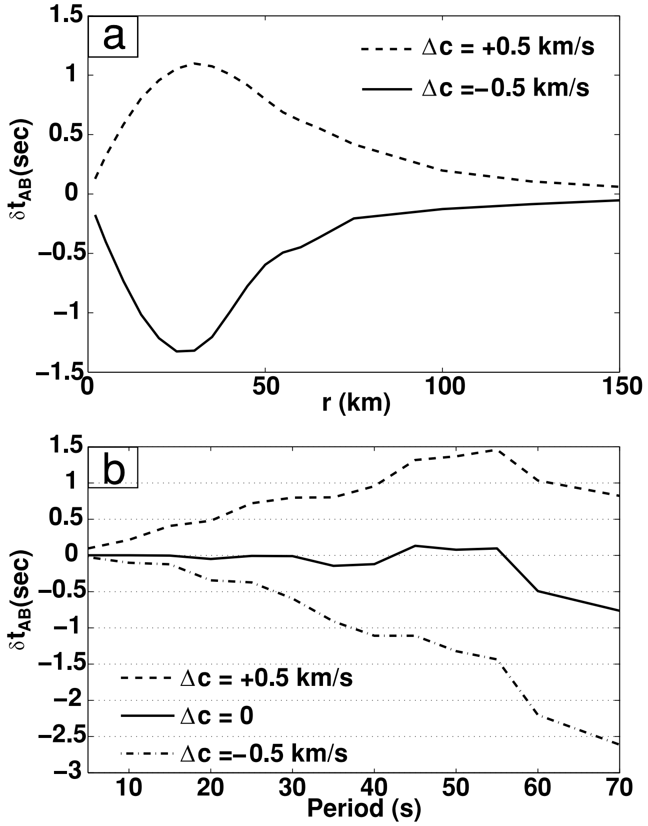

Figure 7. The phase traveltime difference δt_{AB} between the EGF and the theoretical GF for a heterogeneous and isotropic model (Fig. 6) with isotropic ambient noise energy distribution. In (a), we show δt_{AB} as a function of the horizontal scale of the anomaly (r) with the dashed line for a positive anomaly ($\Delta c =$ 0.5 km s^{-1}, case 1 in Fig. 6) and solid line for a negative anomaly ($\Delta c = -0.5$ km s^{-1}, case 2 in Fig. 6). In (b), we fix the horizontal scale of the anomaly $r =$ 50 km and change the period of incoming plane waves. The dashed, solid, and dash-dotted lines show the results for a positive anomaly ($\Delta c = 0.5$ km s^{-1}), no anomaly ($\Delta c = 0$) and a negative anomaly ($\Delta c = -0.5$ km s^{-1}), respectively.

To investigate the dependence on spectral scale (in the data), we fix r at 50 km and let period T increase from 5 to 70 s (Fig. 7b). We set c_0 at 4 km s^{-1} for all periods. For homogeneous and isotropic media (that is $\Delta c = 0$) δt_{AB} is close to zero from $T = 5$ to 55 s (as expected); the negative values for $T > 55$ s reflect the breakdown of far field approximation for surface wave propagation (Yao *et al.* 2006) and, thus, the accuracy of (6). For $\Delta c > 0$ (case 1) δt_{AB} is positive (and $\mu < 0$) and increases as T increases (from 5 to 55 s). For $\Delta c < 0$ (case 2) δt_{AB} is negative (and $\mu > 0$) and the magnitudes of the traveltime and phase velocity biases ($|\delta t_{\mathrm{AB}}|$ and $|\mu|$, respectively) increase with increasing T.

Since the velocity distribution $c(x,y)$ is the same for each period T, the width of the first Fresnel zone increases with increasing T (or wavelength λ) according to (11). The half width of the first Fresnel zone with respect to the two-station path is about 17°, 29° and 38° for $T = 10$, 30 and 50 s, respectively (Fig. 6.) Narrower widths of the first Fresnel zone generally produce smaller bias δt_{AB} and μ between stations A and B, whereas, longer period (longer wavelength) data produces larger differences between EGF and the theoretical GF, which confirms results by Tsai (2009).

In a second experiment we investigate a heterogeneous model (case 1 in Fig. 8) with positive and negative anomalies centred around $(0, -100)$ and $(100, 50)$, respectively. The geometry of the station pair AB is as before, and the ambient noise energy is initially azimuthally isotropic (black line, Fig. 9a). For this model, the relative phase velocity bias at $T = 30$ s reaches -2 per cent for $\varphi = 0°$ and 1 per cent for station pairs with azimuth angle $\varphi \sim 50°$ (Fig. 9c). In general, phase velocities are underestimated for station pairs with high average interstation phase velocities, whereas phase velocities from EGF are overestimated for low velocities (Figs 9b and c). In summary, for isotropic energy distribution, and with asymptotic theory, the strength of phase velocity anomalies (with respect to a constant background) obtained from EGFs is usually underestimated.

3.3.2 Uneven energy distribution

The velocity bias $\mu(\theta)$ produced by uneven energy distribution (black line, Figs 4a and 10a) in the presence of 2-D heterogeneity with and without 5 per cent azimuthal anisotropy (case 1 and 2 in Fig. 8) is presented in Fig. 10(b) (blue line for isotropic medium; red line for the medium with 5 per cent anisotropy). For comparison, the green dotted curve shows the velocity bias for the heterogeneous medium but isotropic plane-wave distribution (Section 3.3.1) and the brown curve shows the bias for the homogeneous medium but uneven plane-wave energy distribution (black line, Fig. 10a). The velocity bias for the heterogeneous (isotropic or anisotropic) medium with uneven plane-wave

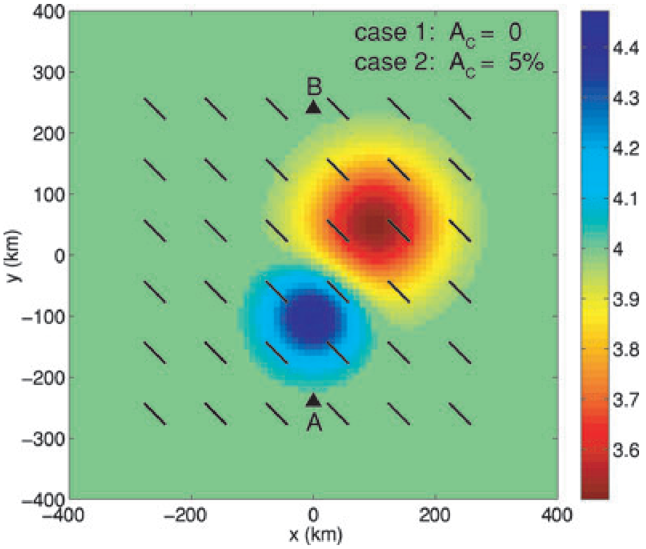

Figure 8. Heterogeneous model (with or without azimuthal anisotropy) for investigating the Green's function retrieval. The velocity model is $c(x, y) = c_0(x, y)\{1 + A_c \cos 2(\theta - \psi)\}$. The colour bar shows the value of the isotropic part of the velocity $c_0(x, y)$(km s^{-1}). The short bars, all with azimuth angle $\psi = 135°$ showing the fast propagation direction, give the azimuthally anisotropic part of the velocity with amplitude $A_c = 0$ for case 1 (no azimuthal anisotropy) and $A_c = 5$ per cent for case 2 (with azimuthal anisotropy).

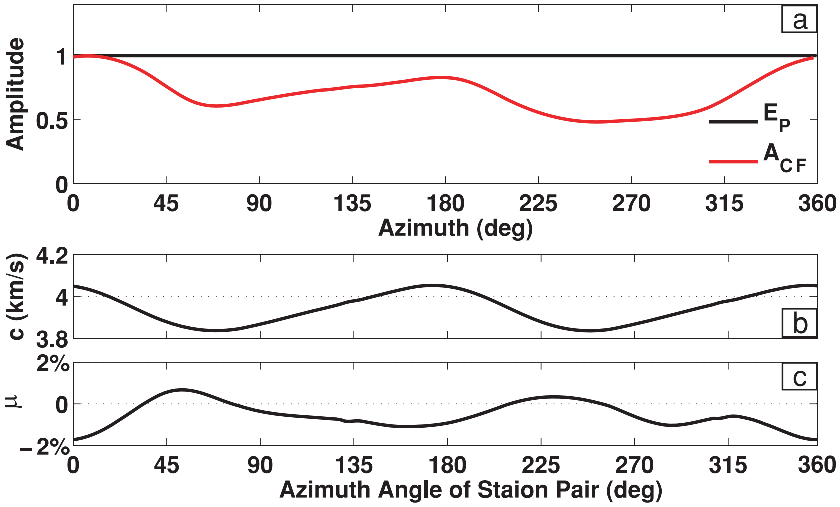

Figure 9. Same as in Fig. 5 with isotropic ambient noise energy distribution in the heterogeneous medium without azimuthal anisotropy (case 1 of the model in Fig. 8).

energy distribution consists of two parts (which are not entirely independent of each other): bias for homogeneous medium with uneven plane-wave energy distribution (brown dashed line, Fig. 10b) and bias for heterogeneous (isotropic or anisotropic) medium with isotropic plane-wave energy distribution (green dashed line, Fig. 10b). Our tests suggest, as before, that the former is generally (much) larger than the latter.

4 RECOVERY OF AMBIENT NOISE ENERGY

4.1 Methodology

In the previous section, we have shown that uneven distribution of ambient noise (plane wave) energy can produce a substantial bias in phase velocities measured from ambient noise interferometry (that is, from EGFs). So far, we have assumed a particular noise energy distribution (e.g. black curve in Figs 4a and 10a). In general, however, we do not know $E_P(\omega, \theta)$ *a priori*. But we do know the interstation cross-correlation functions $C_{AB}(\omega, t)$, or the EGFs inferred from them. The relationship between the amplitudes of $C_{AB}(\omega, t)$ and $E_P(\omega, \theta)$ is non-linear—as shown in (1) and, for instance, Fig. 4(a)—and the former cannot be used as a proxy for the latter. We will show, however, that $E_P(\omega,\theta)$ can be

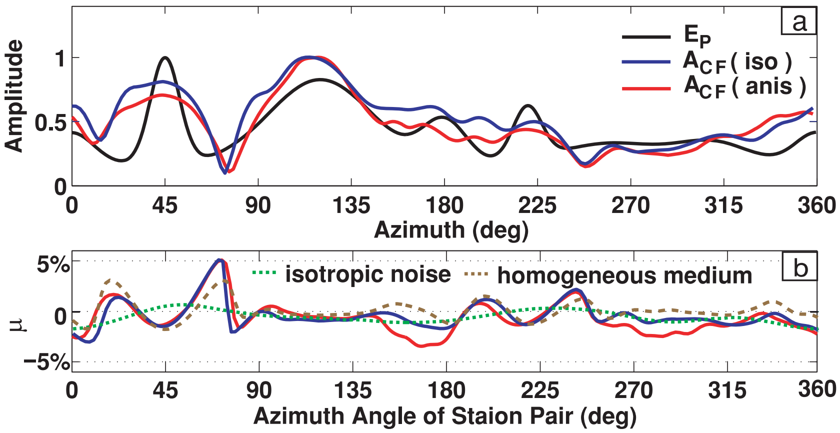

Figure 10. Same as in Fig. 4 with uneven ambient noise energy distribution in the heterogeneous medium as shown in Fig. 8 with blue curves showing the results without azimuthal anisotropy (case 1 in Fig. 8) and red curves showing the results with 5 per cent azimuthal anisotropy (case 2 in Fig. 8). In (b) the green dashed line shows the relative phase velocity bias with isotropic ambient noise energy distribution in the heterogeneous medium (case 1 in Fig. 8), same as the black line in Fig. 9(c). The brown dashed line shows the relative phase velocity bias with uneven ambient noise energy distribution [black curve in (a)] in the homogeneous and isotropic medium with velocity 4 km s^{-1}.

estimated from $C_{\mathrm{AB}}(\omega, t)$ and that the bias in phase velocity measurements from ambient noise interferometry can be quantified and reduced. This involves an inversion, which is here formulated in the context of the plane-wave modelling described in Section 2.

After discretization, eq. (1) in the main surface wave window can be rewritten as

$$C_n(\omega, t, \varphi_n) W_n(t, \Delta_n) = \sum_{m=1}^{M} \mathbf{E}_m(\theta_m) \cos\left[\omega(t - \delta t_{nm})\right] H_{nm}(t, \delta t_{nm}) W_n(t, \Delta_n), \tag{12}$$

where $C_n(\omega, t, \varphi_n)$ is the cross-correlation function for the nth ($n = 1, 2, \ldots, N$) two-station pair with azimuth angle φ_n and interstation distance Δ_n, $W_n(t, \Delta_n)$ the surface wave window function for the nth two-station pair (eq. 7), $\mathbf{E}_m(\theta_m)$ the plane wave energy at the mth azimuth θ_m ($m = 1, 2, \ldots, M$) and δt_{nm} and $H_{nm}(t, \delta t_{nm})$ the phase traveltime difference and cosine taper window function of the nth two-station pair for the mth incoming plane wave, respectively. Taking the Fourier transform for both sides of (12) gives

$$\mathbb{F}\{C_n(\omega, t, \varphi_n) W_n(t, \Delta_n)\} = \sum_{m=1}^{M} \mathbf{E}_m(\theta_m) \mathbb{F}\{\cos\left[\omega(t - \delta t_{nm})\right] H_{nm}(t, \delta t_{nm}) W_n(t, \Delta_n)\}. \tag{13}$$

Separation of the real and imagery parts (at frequency ω) gives the following matrix equation:

$$\mathbf{A}_R + j\mathbf{A}_S = (\mathbf{R} + j\mathbf{S})\mathbf{E}, \tag{14}$$

where j is the imaginary unit, $\mathbf{A}_R$ and $\mathbf{A}_S$ $N \times 1$ dimensional vectors, $\mathbf{R}$ and $\mathbf{S}$ $N \times M$ dimension matrices, and $\mathbf{E}$ an $M \times 1$ dimension vector

$$\begin{aligned}
(\mathbf{A}_R)_n &= \mathrm{Re}\left(\mathbb{F}\{C_n(\omega, t, \varphi_n) W_n(t, \Delta_n)\}\right)\big|_\omega \\
(\mathbf{A}_S)_n &= \mathrm{Im}\left(\mathbb{F}\{C_n(\omega, t, \varphi_n) W_n(t, \Delta_n)\}\right)\big|_\omega \\
\mathbf{R}_{nm} &= \mathrm{Re}\left(\mathbb{F}\{\cos\left[\omega(t - \delta t_{nm})\right] H_{nm}(t, \delta t_{nm}) W_n(t, \Delta_n)\}\right)\big|_\omega \\
\mathbf{S}_{nm} &= \mathrm{Im}\left(\mathbb{F}\{\cos\left[\omega(t - \delta t_{nm})\right] H_{nm}(t, \delta t_{nm}) W_n(t, \Delta_n)\}\right)\big|_\omega \\
\mathbf{E}_m &= \mathbf{E}_m(\theta_m),
\end{aligned} \tag{15}$$

with $\mathrm{Re}(\cdots)|_\omega$and $\mathrm{Im}(\cdots)|_\omega$ operators that take the real and imaginary part at frequency ω.

We note that eq. (14) is linear between data ($\mathbf{A}_R$ and $\mathbf{A}_S$) and model parameters $\mathbf{E}$ because of the linear property of the Fourier transform. Therefore, $\mathbf{E}$ can be solved from $\mathbf{A}_R$ and $\mathbf{A}_S$ through a least-squares inversion scheme. However, the energy or amplitude of the windowed cross-correlation function is non-linearly dependent on $\mathbf{E}$ as inferred from (13) and (14). To obtain, by inversion, the ambient noise energy vector $\mathbf{E}$ we define the penalty function $\chi(\mathbf{E})$

$$\chi(\mathbf{E}) = (\mathbf{RE} - \mathbf{A}_R)^T(\mathbf{RE} - \mathbf{A}_R) + (\mathbf{SE} - \mathbf{A}_S)^T(\mathbf{SE} - \mathbf{A}_S) + \lambda_D(\mathbf{DE})^T(\mathbf{DE}), \tag{16}$$

where the superscript ^{T} denotes the transpose of a matrix, λ_D a damping parameter, and $\mathbf{D}$ an $(M - 1) \times M$ dimension smoothing operator (first finite difference matrix) defined as

$$\mathbf{D} = \begin{bmatrix} -1 & 1 & 0 & \dots & \dots & 0 \\ 0 & -1 & 1 & \dots & \dots & 0 \\ & & \dots & \dots & & \\ & & & \dots & \dots & \\ 0 & \dots & \dots & -1 & 1 & 0 \\ 0 & \dots & \dots & 0 & -1 & 1 \end{bmatrix}.$$

On the right-hand side of (16) the first and second terms give the data misfit for the real and imaginary parts as shown in (14), respectively, and the third term denotes model roughness. Optimization of this equation, that is, solving for $\partial\chi(\mathbf{E})/\partial\mathbf{E} = 0$, gives the solution

$$\mathbf{E} = \left(\mathbf{R}^T\mathbf{R} + \mathbf{S}^T\mathbf{S} + \lambda_D\mathbf{D}^T\mathbf{D}\right)^{-1}\left(\mathbf{R}^T\mathbf{A}_R + \mathbf{S}^T\mathbf{A}_S\right). \tag{17}$$

Eq. (17) shows how the distribution of ambient noise energy can be estimated from the real and imaginary parts of the Fourier transformed cross-correlation functions.

4.2 Proof of concept

To illustrate the inversion for ambient noise energy $\mathbf{E}$ we use the same station geometry as before, with station azimuth φ (from A to B) varying from 0° to 358° with $\mathrm{d}\varphi = 2°$ so that the number of data (cross-correlations) $N = 180$. For the discretization in (12) we use $\mathrm{d}\theta = 0.5°$ to ensure enough sampling of plane waves for the GF recovery. Inverting for $\mathbf{E}$ at $\mathrm{d}\theta = 0.5°$ intervals would imply 720 unknowns ($M \gg N$). In order to reduce the number of unknowns (to $K = 90$), however, we invert for $\tilde{\mathbf{E}}$ at 4° interval (that is, $\tilde{\theta}_k = 0°, 4°, \ldots, 356°$). For any incoming plane wave with azimuth $\theta_m (0 \le \theta_m < 360°)$, there exists a number k such that $\tilde{\theta}_k \le \theta_m < \tilde{\theta}_{k+1}$ and the energy $\mathbf{E}_m$ is linearly interpolated between $(\tilde{\mathbf{E}})_k$ and $(\tilde{\mathbf{E}})_{k+1}$ as

$$\begin{aligned} \mathbf{E}_m &= \beta_{mk}\left(\tilde{\mathbf{E}}\right)_k + \beta_{m(k+1)}(\tilde{\mathbf{E}})_{k+1} \\ \beta_{m(k+1)} &= (\theta_m - \tilde{\theta}_k)/(\tilde{\theta}_{k+1} - \tilde{\theta}_k) \\ \beta_{mk} &= (1 - \beta_{m(k+1)}), \end{aligned} \tag{18}$$

or in a matrix form as

$$\mathbf{E} = \beta\tilde{\mathbf{E}}, \tag{19}$$

with $\boldsymbol{\beta}$ an $M \times K$ matrix with elements β_{mk}; if $\theta_m \ge \tilde{\theta}_K = 356°, \tilde{\theta}_{K+1} = 360°$ and $(\tilde{\mathbf{E}})_{K+1} = \left(\tilde{\mathbf{E}}\right)_1$. Substituting (18) into (14) and reformatting it, we obtain $\mathbf{A}_R + j\mathbf{A}_S = (\tilde{\mathbf{R}} + j\tilde{\mathbf{S}})\tilde{\mathbf{E}}$, with $\tilde{\mathbf{R}}$ and $\tilde{\mathbf{S}}$ $N \times K$ dimensional matrices defined as

$$\begin{aligned} \tilde{\mathbf{R}} &= \mathbf{R}\beta \\ \tilde{\mathbf{S}} &= \mathbf{S}\beta. \end{aligned} \tag{20}$$

Therefore, the solution sought is

$$\tilde{\mathbf{E}} = \left(\tilde{\mathbf{R}}^T\tilde{\mathbf{R}} + \tilde{\mathbf{S}}^T\tilde{\mathbf{S}} + \lambda_D\mathbf{D}^T\mathbf{D}\right)^{-1}\left(\tilde{\mathbf{R}}^T\mathbf{A}_R + \tilde{\mathbf{S}}^T\mathbf{A}_S\right). \tag{21}$$

We test this inversion scheme with the same noise energy distribution as before (black lines in Fig. 4a). We calculate the $N = 180$ cross-correlation functions using (1) and take the real and imaginary parts, that is,$\mathbf{A}_R$ and A_S, as in (15). With $\delta t_{nm} = \delta\phi_{nm}/\omega$, where $\delta\phi_{nm}$ is the phase delay in (4), we obtain $\tilde{\mathbf{R}}$ and $\tilde{\mathbf{S}}$ from (15) and (20). Finally, we obtain estimates of the azimuthal distribution of ambient noise energy $\tilde{\mathbf{E}}$ from (21) for different damping parameters λ_D.

For a homogeneous and isotropic medium (as in Section 3.1) we can recover the ambient noise energy (magenta circles, Fig. 11a) without damping, that is, $\lambda_D = 0$. For a heterogeneous, isotropic medium (Fig. 8, case 1) the undamped solution (magenta circles, Fig. 11b) is unstable, but $\tilde{\mathbf{E}}$ is identical to distribution $\mathbf{E}$ for $\lambda_D = 100$ (blue circles, Fig. 11b). If the medium is azimuthally anisotropic (we added 5 per cent anisotropy, as in Fig. 8, case 2) $\mathbf{E}$ can still be recovered but stronger damping is needed to stabilize the solution (Fig. 11c).

The above examples demonstrate that ambient noise energy $E_P(\omega, \theta)$ can be recovered from data, that is the cross-correlations. We have, however, used the same model in the forward problem as in the inversion, whereas in practice the input model, for example, phase velocity maps (Yao *et al.* 2006), will be an estimate of the true model. We recall that measurements (EGFs) are influenced by a combination of uneven ambient noise energy distribution and medium complexity (heterogeneity and anisotropy). The influence from medium complexity is a consequence of our assumption of plane-wave sources, and is generally smaller than that from noise energy distribution (Section 3). To assess the recovery of $E_P(\omega, \theta)$ when the input model for inversion is different from (but close to) the true model we calculate cross-correlation functions from one model (Fig. 8, case 2) and perform the inversion with another (Fig. 12a). The fact that recovery (blue circles, Fig. 12b) is satisfactory motivates the following three-step approach. First, we use the phase velocity maps obtained by inversion of the original (uncorrected) data from the recovered EGFs (e.g. Yao *et al.* 2006) to estimate the spatial distribution of ambient noise energy. Second, we use this estimate of the noise energy distribution to calculate (and remove) the bias in phase velocities. Third, we use the corrected phase velocities for final unbiased inversion. (This loop can be repeated, but our simulations suggest that a single iteration is sufficient.)

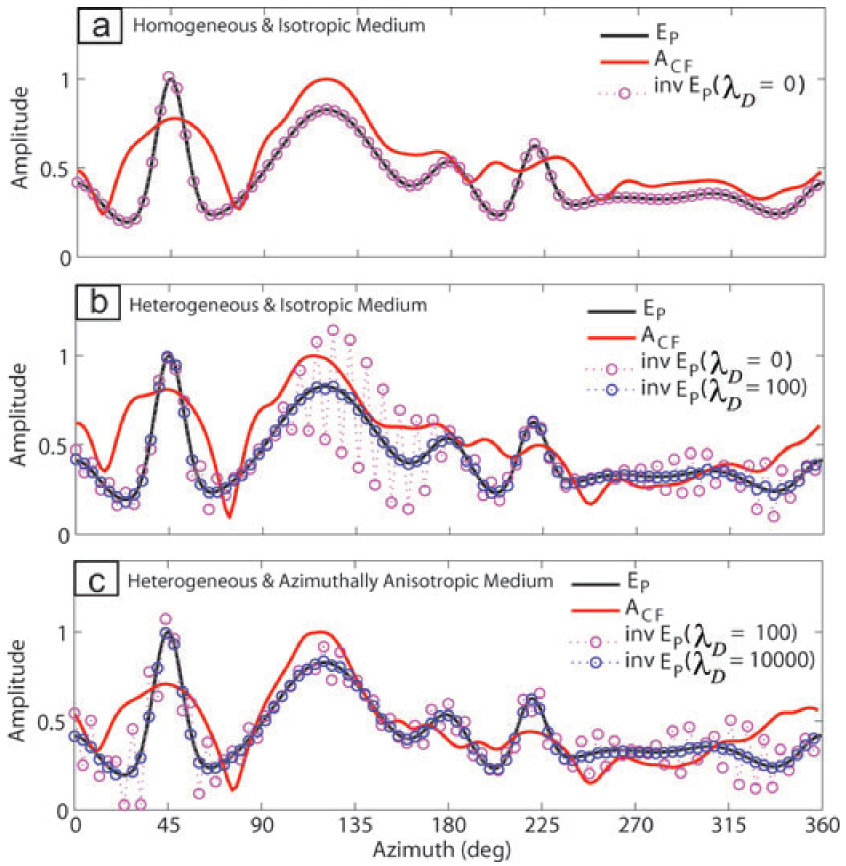

Figure 11. Recovery of the azimuthal distribution of ambient noise energy (magenta or blue open circles) from the cross-correlation functions as described in Section 4 for (a) the homogeneous and isotropic medium (Section 3.1) without adding damping ($\lambda_D = 0$), (b) the heterogeneous medium without azimuthal anisotropy (case 1 in Fig. 8) with the damping values $\lambda_D = 0$ (for the magenta circles) and $\lambda_D = 100$ (for the blue circles) and (c) the heterogeneous medium with 5 per cent azimuthal anisotropy (case 2 in Fig. 8) with the damping values $\lambda_D = 100$ (for the magenta circles) and $\lambda_D = 10000$ (for the blue circles). The input ambient noise energy E_P is shown as the black line. The red line shows the amplitude of the cross-correlation functions.

5 APPLICATION IN SE TIBET AND AZIMUTHAL ANISOTROPY

We use one month of vertical component data from the seismograph array in SE Tibet (Fig. 13a) to illustrate the process of recovery of ambient noise energy, estimation of phase velocity bias, and inversion for velocity model using an iterative procedure. We show the difference of the isotropic phase velocity map and azimuthal anisotropy before and after the correction of phase velocity bias.

5.1 Iterative procedure

We obtain $C_{AB}(\omega, t)$ for all possible two-station pairs (Fig. 13c) by one-bit cross-correlation of vertical component data recorded at A and B in the period band 10–30 s—see Yao *et al.* (2008) for details about data processing. To obtain more symmetric (reciprocal) EGFs from the cross-correlation functions $C_{AB}(\omega, t)$ we use eq. (5) and stack, for each station pair, the causal and anticausal parts of the EGFs. We refer to this stack as the symmetric component. From the resulting EGF we measure the phase velocities $\tilde{c}_{AB}$ using the method by Yao *et al.* (2006). This assumes perfect recovery of GF in a far field, but—as discussed in Section 3—the obtained dispersion data may be biased due to uneven noise distribution and structure complexity. We use the following iterative procedure to estimate the ambient noise energy distribution, phase velocity bias and 2-D phase velocity distribution at certain period T.

Step 1: Invert for 2-D phase velocity map (isotropic or azimuthally anisotropic) using interstation phase velocity measurements $c^{(k)}$ ($k = 1, 2, \ldots$; $k = 1$ for the original measurements $\tilde{c}_{AB}$ from symmetric component EGFs, and $k > 1$ for updated phase velocities in Step 3 after bias correction in each iteration)

Step 2: Estimate ambient noise (plane-wave) energy distribution $\tilde{\mathbf{E}}^{(k)}$ by means of plane-wave modelling (Section 4). As point of departure for the modelling we use the 2-D phase velocity maps from Step 1, and we use both the causal and anticausal part of the cross-correlation functions to obtain the data $\mathbf{A}_R$ and $\mathbf{A}_S$ in (15), with the requirement that the interstation distance is at least 2 wavelengths.

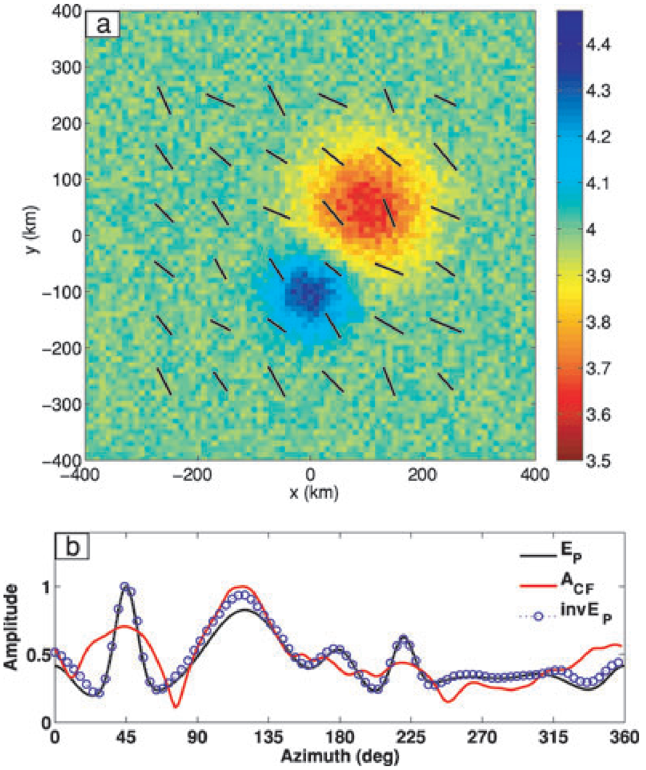

Figure 12. (a) A modified velocity model for the modelling in the inversion using eq. (21). The original velocity model is shown as the case 2 of the model in Fig. 8, which is used for the calculation of the cross-correlation functions from eq. (1). The amplitude of the velocity anomaly (isotropic part) in the modified model is 75 per cent of that in the original velocity model. And a maximum of 0.05 km s^{-1} random noise is added to the isotropic part of the modified velocity model. For the azimuthal anisotropic part, we add a maximum of 25° random noise to the azimuth of the fast propagation direction and a maximum of 2 per cent random noise to the amplitude of azimuthal anisotropy (originally 5 per cent). (b) Recovery of the ambient noise energy (blue open circles) when using the modified velocity model (a) in the inversion but the original velocity model for calculating the cross-correlation functions. In (b), the input ambient noise energy is shown as the black curve and the red curve shows the amplitude of the cross-correlation functions.

Step 3: Estimate the relative phase velocity bias $\mu^{(k)}$ between the EGF and theoretical GF defined in (9) and update the phase velocity measurements with

$$c^{(k+1)} = \tilde{c}_{\mathrm{AB}}/(1+\mu^{(k)}). \tag{22}$$

Since we use the symmetric component EGFs for dispersion analysis, the phase delay between the EGF and GF expressed as eq. (8) can be modified as

$$\delta\phi_{\mathrm{AB}}(\omega) = \Theta\{[\tilde{G}_{\mathrm{AB}}(\omega,t) + \tilde{G}_{\mathrm{BA}}(\omega,t)]W(t,\Delta_{\mathrm{AB}})\} - \Theta[G_{\mathrm{AB}}(\omega,t)W(t,\Delta_{\mathrm{AB}})]. \tag{23}$$

Note that we still use the 2-D phase velocity map from Step 1 for plane-wave modelling and for calculating the EGF and theoretical GF.

Step 4: If $c^{(k+1)}$ or $\tilde{\mathbf{E}}^{(k)}$ converges, stop iteration; otherwise go back to Step 1.

We emphasize that the obtained ambient noise energy distribution $\tilde{\mathbf{E}}^{(k)}$ depends on the normalization involved in cross-correlation (here we use one-bit cross-correlation). In view of the relationship between the cross-correlation function and ambient noise energy (eqs (1) and (13)), $\tilde{\mathbf{E}}^{(k)}(\theta)$ measures the overall normalized energy of the incoming plane waves at azimuth θ in the entire period of cross-correlation, which, in our example, is one month. This linearity also implies that the overall noise energy in a longer time window can be obtained through summation of noise energy in shorter time windows.

The convergence depends on the quality of the first preliminary phase velocity map from ambient noise tomography. If it is close to the real model, we may expect convergence after one or two iterations. During the iterative process we can simultaneously invert for azimuthal anisotropy and the isotropic part of phase velocity maps. In the examples shown below we consider isotropy for the first two iterations (i.e. $k = 1, 2$) and subsequently ($k = 3, 4, \ldots$) invert for azimuthally anisotropic phase velocity at the period $T = 25$ s. The corresponding ray path coverage at $T = 25$ s is shown as Fig. 13(b).

5.2 Results

In Fig. 14(a), we show the estimated ambient noise (plane-wave) energy distribution $\tilde{\mathbf{E}}^{(k)}$ for the first four iterations, which is similar to the azimuth-dependent normalized amplitudes of cross-correlation functions for all possible MIT array station pairs (see Fig. 14b). The maximum

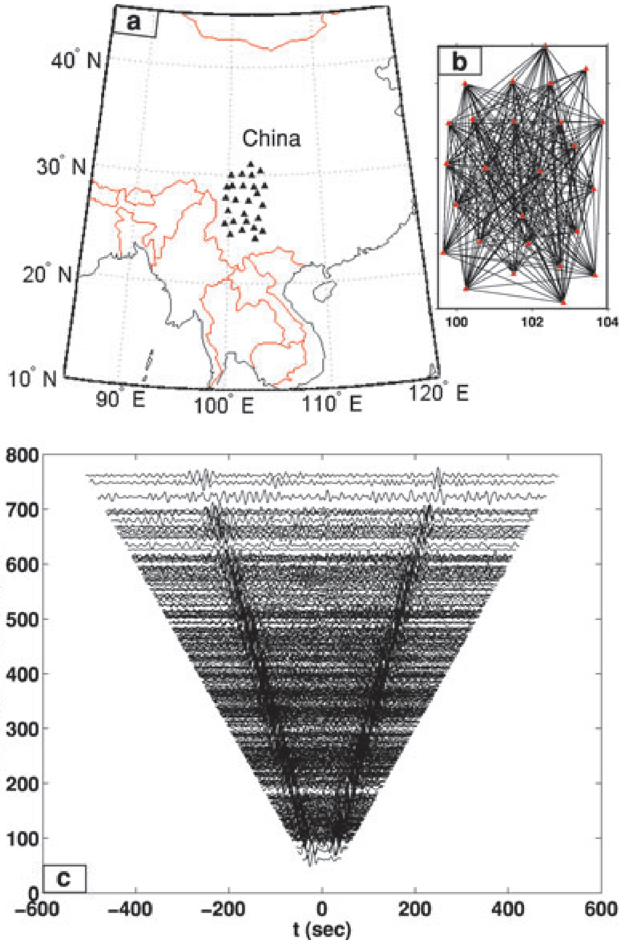

Figure 13. (a) Location of the MIT array in SE Tibet, China. (b) Ray path coverage for interstation phase velocity measurements at $T = 25$ s from the EGFs retrieved from one month data (2004 January) of the MIT array. (c) All interstation cross-correlation functions in the period band 10–30 s from one-bit cross-correlation of one month MIT array data (2004 January). The maximum amplitude of each trace is normalized for display purposes.

noise energy with respect to the array appears between the azimuth angle 90°–135°, which is about to the ESE of the array, pointing towards the oceans. The first two iterations, based on the isotropic phase velocity maps, yield similar values of $\tilde{\mathbf{E}}^{(k)}$ almost at all azimuth angles. Similar results are obtained for the third and fourth iterations, which are based on azimuthally anisotropic phase velocity maps. The incorporation of azimuthal anisotropy yields slight differences in $\tilde{\mathbf{E}}^{(k)}$ at some azimuth angles. This result suggests that one iteration is enough to obtain stable estimation of ambient noise energy both for isotropic and azimuthally anisotropic media. During the inversion for $\tilde{\mathbf{E}}^{(k)}$, an appropriate value of the damping parameter λ_D need to be set. Using an automated scheme, we determine λ_D from the trade-off curve (upper left-hand inset figure in Fig. 14a) between the data misfit [$d_{\text{misfit}} = (\tilde{\mathbf{R}}\tilde{\mathbf{E}} - \mathbf{A}_R)^T(\tilde{\mathbf{R}}\tilde{\mathbf{E}} - \mathbf{A}_R) + (\tilde{\mathbf{S}}\tilde{\mathbf{E}} - \mathbf{A}_S)^T(\tilde{\mathbf{S}}\tilde{\mathbf{E}} - \mathbf{A}_S)$, modified from the first two terms of (16)] and the model roughness [$m_{\text{rough}} = (\mathbf{D}\tilde{\mathbf{E}})^T(\mathbf{D}\tilde{\mathbf{E}})$, modified from the third term of (16)]. We try a broad range of values for λ_D from 0 to $\mathbf{A}_R^T\mathbf{A}_R + \mathbf{A}_S^T\mathbf{A}_S$ (open circles in the inset figure of Fig. 14a) to obtain the trade-off curve by interpolation. On the trade-off curve we find λ_1 such that $d_{\text{misfit}}(\lambda_1) = 0.15\,\max(d_{\text{misfit}})$ and λ_2 such that $m_{\text{rough}}(\lambda_2) = 0.15\,\max(m_{\text{rough}})$. The value of λ_D for the final inversion of $\tilde{\mathbf{E}}$ is set, empirically, to $\lambda_D = 10^{0.5(\log_{10}\lambda_1 + \log_{10}\lambda_2)}$. The λ_D selected this way yields a smooth $\tilde{\mathbf{E}}$ and also a small data misfit from our tests.

Fig. 15 shows the relative interstation phase velocity bias $\mu^{(k)}$ from EGFs for two periods $T = 10$ s (Figs 15a–d) and $T = 25$ s (Figs 15e–h) as a function of interstation distance (left-hand column) or azimuth (right-hand column) for the isotropic or azimuthally anisotropic case. As expected, the bias $\mu^{(k)}$ depends on azimuth (Figs 15b, d, f and h). For example, the systematic bias $\mu^{(k)}$ for the paths with azimuth angles 90°–135° (Figs 15f and h) is mainly due to the large variation of ambient noise energy between 90° and 135° (Fig. 14). For most paths the bias is less than 1 per cent, probably because we use the symmetric component EGFs, which creates a more isotropic noise distribution. The magnitude of the bias decreases with increasing interstation distance (Figs 15a, c, e and g). This is mainly because that the width of the first Fresnel zone for interferometry decreases as the interstation distance increases. As a consequence, the final construction of GF will be less sensitive to the (relatively long wavelength) variation of ambient noise energy and medium heterogeneity. This effect is similar to the decrease in phase velocity bias due to a decrease in wavelength (and, thus, Fresnel zone width) discussed in Section. 3.3.1. Indeed, the bias at $T = 10$ s (Figs 15a and c) is smaller than at $T = 25$ s (Figs 15e and g). Consistent with the outcome of the modelling experiments (Section 3), the incorporation of (weak) azimuthal anisotropy has only a small effect on the estimation of bias for most paths (e.g. comparing results between Figs 15b and d, or Figs 15f and h).

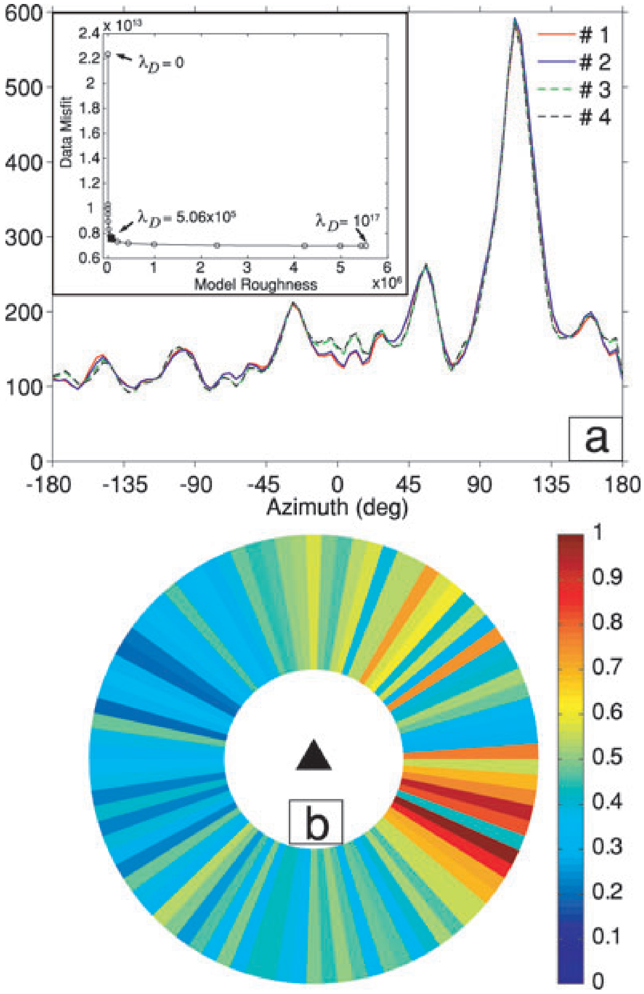

Figure 14. (a) Inversion results of azimuth-dependent ambient noise energy distribution at $T = 25$ s with respect to the MIT array using plane-wave modelling and an iterative approach. The results for the first four iterations are shown as the red, blue, green dashed and black dashed lines, respectively. The first two iterations are based on the isotropic phase velocity maps and the third and fourth iterations use the azimuthally anisotropic phase velocity maps. In the upper left-hand inset figure in (a), we show the trade-off curve between the data misfit and model roughness (defined in Section 5.2). The open circles show the trial damping values in the inversion and the black solid square shows the final choice of damping value for the inversion of ambient noise energy. (b) Azimuthal dependence of the normalized amplitudes of the cross-correlation functions (bandpass filtered between 23 and 27 s) for all possible MIT array station pairs. The pie charts are constructed using the procedure from Stehly *et al.* (2006) by averaging the amplitude of all cross-correlation functions in each azimuthal sector (5° width here) with a geometrical spreading amplitude correction considering the difference in interstation distance. The colour bar in the right-hand side gives the value of normalized amplitude. Note that the inversion results of ambient noise energy distribution (a) are similar to the azimuthal distribution of normalized amplitudes of the cross-correlation functions. The maximum noise energy appears between the azimuth 90°–135°, which is about to the ESE of the array and points towards the oceans.

Fig. 16 shows the phase velocity maps at $T = 25$ s obtained from the original, uncorrected phase velocity measurements $\tilde{c}_{\mathrm{AB}}$ and from the corrected measurements $c^{(k)}$. Using $\tilde{c}_{\mathrm{AB}}$, we first perform inversions for isotropic and anisotroic phase velocity maps (Figs 16a and b) using the regionalization due to Montagner (1986). For the anisotropy inversion, the phase velocity at each grid point is expressed as $c(x, y) = c_0(x, y)\{1 + A(x, y)\cos(2\psi) + B(x, y)\sin(2\psi)\}$, where $c_0(x, y)$ is the transversely isotropic part of the phase velocity, $A(x, y)$ and $B(x, y)$ are the azimuthally anisotropic terms, and ψ is the azimuth of the ray path through (x, y). The isotropic part of the inversion that also allows for azimuthal anisotropy (Fig. 16b) is very similar to the map from the inversion that considers only isotropy (Fig. 16a), which implies that the trade-off between isotropic phase velocities $c_0(x, y)$ and azimuthally anisotropic terms $A(x, y)$ and $B(x, y)$ is small (see also Simons *et al.* 2002). In Fig. 16(c), we show the azimuthally anisotropic phase velocity map using the corrected interstation phase velocities $c^{(k)}$ after four iterations as given above, which is generally similar to the results using the uncorrected measurements $\tilde{c}_{\mathrm{AB}}$ (Fig. 16b). The largest difference in isotropic phase velocity before and after bias correction is about 1 per cent, which is much smaller than the variation of phase velocity map at this period (>10 per cent). The pattern and magnitude of the azimuthal anisotropy are also similar and the difference is probably less than the uncertainty in the inversion results. Inversions for other periods yield similar results. In particular, the pattern and magnitude of azimuthal anisotropy at 10 s are almost the same before and after bias correction.

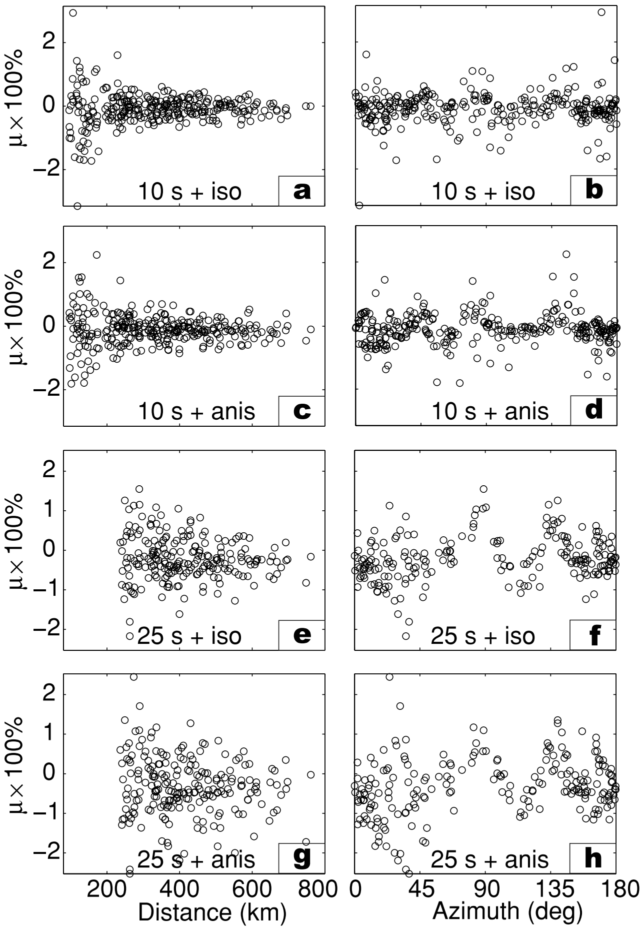

Figure 15. Relative bias (μ) of phase velocities between the EGF and GF versus interstation distance (left-hand column) or azimuth (right-hand column) for the periods $T = 10$ s (a–d) and $T = 25$ s (e–h) using either isotropic phase velocity maps (a, b, e, f) or azimuthally anisotropic phase velocity maps (c, d, g, h) for the forward (plane-wave) modelling.

6 DISCUSSION

Ambient noise tomography has become an important tool for investigations of the structure of the crust and shallow mantle lithosphere using data from seismograph array stations. However, the surface wave GFs are generally not fully reconstructed due to uneven distribution of ambient noise sources. This raises the concern that dispersion measurements from such EGFs are biased, which can degrade the accuracy of ambient noise tomography, especially for anisotropic structure.

We have investigated this problem under the assumption of plane wave propagation (that is, asymptotic theory). In particular, the theoretical GFs used here are evaluated with a ray theoretical approximation. The approach presented here is generally applicable for ambient noise array tomography if: (1) the waves generated from distant noise sources can be approximated as plane waves propagating across the array (that is, the horizontal scale of the study region must be relatively small compared to the distance to the main noise sources—for example, ocean microseisms—and the energy of local scattered surface waves must be much weaker than that of faraway sources); (2) there is good azimuth coverage of two-station paths and (3) an adequate initial model for plane wave modelling is available.

The small-scale array in the first requirement is generally satisfied for most regional ambient noise array tomographic studies, for example, in SE Tibet (Yao *et al.* 2006, 2008), New Zealand (Lin *et al.* 2007), South Korea (Kang & Shin 2006), and southern California (Shapiro *et al.* 2005). For ambient noise tomography, the period range is typically within 10–40 s, for which the ambient noise is generated mainly through ocean wave activities (e.g. storms) generated in the northern oceans during the northern hemisphere winter and in the southern oceans during the northern summer (e.g. Stehly *et al.* 2006; Rhie & Romanowicz 2006). It is still under debate whether the seismic noise for periods larger than 10 s is related to ocean wave activity in deep water (Stehly *et al.* 2006) or generated by the non-linear interaction of ocean waves with seafloor near coastlines (Yang & Ritzwoller 2008a). Such nearby noise sources may invalidate plane wave modelling, especially at short periods ($<$10 s) and for near-coastal arrays due to non-linear interactions of ocean waves with coastlines in the secondary microseism band (5–10 s) (e.g. Stehly *et al.* 2006). For near coastal arrays, for instance, in southern Italy, ambient noise sources can be near coastline in the primary microseism band (10–20 s) based on migration analysis (Brzak *et al.* 2008). Therefore, in these cases, effects on the GF recovery from near sources are important, which can be possibly accounted for by adding extra near source terms to (1) and (12). However, plane-wave beamforming analysis (Yao *et al.* 2009) demonstrates that ambient noise energy in the primary microseism band (10–20 s) propagating into

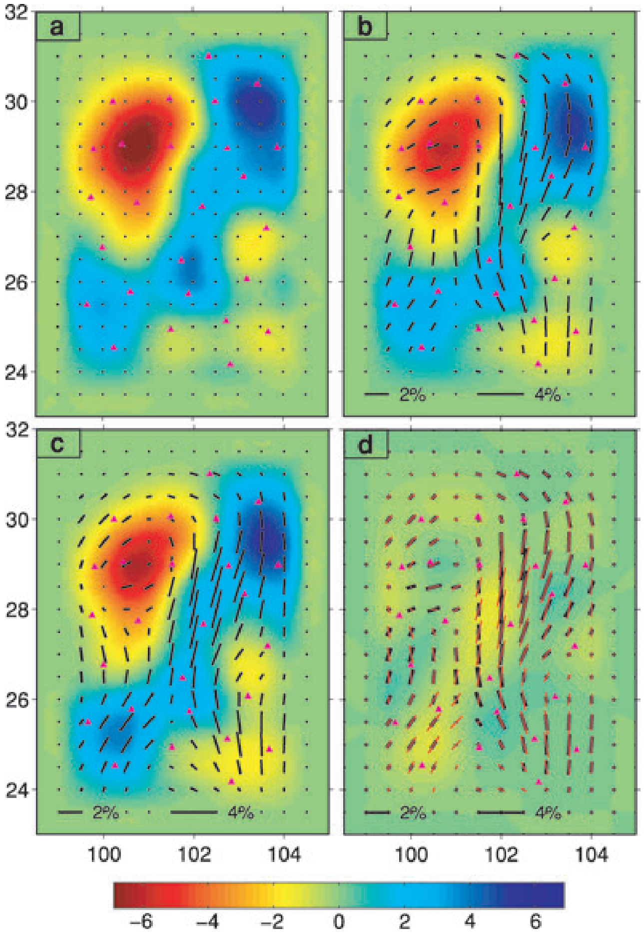

Figure 16. Distribution of 2-D phase velocity maps (in per cent with respect to the average value) at $T = 25$ s using (a) uncorrected phase velocity measurements without azimuthal anisotropy inversion, (b) uncorrected phase velocity measurements with azimuthal anisotropy inversion, and (c) corrected phase velocity measurements with azimuthal anisotropy inversion as described in Section 2. The background image of (d) shows the difference (in per cent) of phase velocities between the isotropic part of phase velocity maps of (b) and (c). On (d) the thick black bars and red thin bars show the comparison of azimuthal anisotropy from (b) and (c), respectively. The colour bar gives the magnitude of perturbation (in per cent) of isotropic phase velocities and the two horizontal bars at the bottom of (b–d) gives the magnitude of azimuthal anisotropy.

the array in SE Tibet correlates well with distant ocean wave activity with seasonal variations. Since the array in SE Tibet is at least about one thousand kilometres away from the coastline, even if there exist near coastal sources, plane wave approximation is still a good approximation to represent energy propagation through this small array. The requirement that local scattering is small compared to the energy from distant noise sources is not easily verified. For the array in SE Tibet, however, the dominant sources (after one-bit normalization of data) are ocean microseisms, with much weaker contributions from local scattering (Yao *et al.* 2009).

The second and third requirements are needed to ensure robust estimation of the azimuthal distribution of ambient noise energy. For seismic arrays with good spatial and azimuthal interstation path coverage, such as the MIT array in SE Tibet (Yao *et al.* 2008), we can usually estimate noise energy at azimuth intervals of several degree. However, for seismic arrays with a narrow azimuthal path coverage, such a 2-D arrays with a large aspect ratios, the estimation of azimuthal energy distribution will be less reliable. As input velocity model for the plane wave modelling one can use the isotropic phase velocity maps from ambient noise tomography without bias correction.

We note that in heterogeneous media the true (full wave) GF may be slightly different, with the difference expected to be dependent on the scale of the medium. The simplified approach presented here is relevant, however, because most current ambient noise (surface wave) tomography studies similarly rely on asymptotic theory (e.g. ray paths, phase velocity maps). There is no fundamental obstruction to extend the same concept to full wave theory, with the use of full wave sensitivity kernels, but that would only be useful if the entire tomographic inversion is posed as a full wave, multiscale problem (with model parameters inferred directly from broad-band data and not from phase or group velocity maps).

Our analysis suggests that ambient noise tomography for isotropic wave speed variations is likely to be robust (that is, it is relatively insensitive to bias due to incomplete GF reconstruction) if one uses long time windows (e.g. several months or even 1 yr) for cross-correlation and the symmetric component EGF (the sum of the causal and anticausal part of EGF) for dispersion analysis (e.g. Yang *et al.* 2008; Yao *et al.* 2008). For the MIT array in SE Tibet the phase velocity bias is generally less than 1 per cent, which is small compared to the inferred wave speed variations and which causes a very small effect on the isotropic phase velocity maps in the wave period of interest

($T = 10$–30 s). The azimuthal dependence of phase velocity bias is a bigger concern for inversions for (azimuthally) anisotropic structure. Our example in SE Tibet shows, however, that this effect is generally small, and the (spatial) smoothing employed in surface wave tomography further suppresses any effects of azimuth-dependent bias.

Even if the effect is small for our array in SE Tibet, we recommend that inversions for azimuthal anisotropy are subjected to bias analysis if the EGFs indicate that the distribution of ambient noise energy varies rapidly with azimuth. The azimuth dependence can also be quantified by means of beam forming (Harmon *et al.* 2008; Yao *et al.* 2009). Similar in concept to other differential methods, if ambient noise sources generate both Love and Rayleigh waves, radial anisotropy inferred from the discrepancy between Love and Rayleigh wave GFs is less sensitive to the actual distribution of ambient noise energy. If Love and Rayleigh waves are excited by different source distributions, however, careful analysis of phase velocity bias for both Love and Rayleigh dispersion is necessary to constrain radial anisotropy.

We note that our plane-wave modelling approach assumes a lossless medium; that is, it ignores the effect of attenuation on the amplitude of waves. We emphasize, however, that even without attenuation there will be an apparent decay of amplitude of EGFs due to the fact that the width of the first Fresnel zone for constructive interference decreases as the increase of interstation distance (see also Harmon *et al.* 2007). Recent studies (Prieto & Beroza 2008; Prieto *et al*. 2009) show that it is possible to extract anelastic (attenuation) structure from ambient noise interferometry, provided that the noise energy distribution is isotropic. Since the noise energy distribution is generally not isotropic, our inversion approach for estimating the ambient noise energy distribution could help interferometric quantification of medium attenuation.

7 SUMMARY

We have presented a method for estimating the distribution of ambient noise energy and the bias in phase velocities from ambient noise interferometry under the assumption of plane wave propagation. Through an iterative approach we correct the phase velocity measurements from EGFs and estimate the azimuthal anisotropy of surface wave propagation with more confidence. Our method can be applied to small-scale arrays with good spatial and azimuthal path coverage and which are located far from the dominant noise sources. With real application to SE Tibet, we find the azimuthal variation of ambient noise energy has very small effect on the isotropic and azimuthally anisotropic phase velocities in SE Tibet.

ACKNOWLEDGMENTS

We thank the Editor Jeannot Trampert and an anonymous reviewer for their constructive comments, which helped us improve the manuscript. We also thank Professor Jean-Paul Montagner at IPGP for providing the code for inversion of surface wave azimuthal anisotropy and Dr Victor Tsai at Harvard for helpful discussions. This work was supported by US AFRL grants FA8718–07-C-0001.

REFERENCES

Bensen, G.D., Ritzwoller, M.H., Barmin, M.P., Levshin, A.L., Lin, F., Moschetti, M.P., Shapiro, N.M. & Yang, Y., 2007. Processing seismic ambient noise data to obtain reliable broad-band surface wave dispersion measurements, *Geophys. J. Int.,* **169,** 1239–1260.

Brzak, K., Gu, Y.J., Ökeler, A., Stechler, M. & Lerner-Lam, A., 2008. Migration imaging and forward modeling of microseismic noise sources near southern Italy, *Geochem. Geophys. Geosyst.,* **10,** Q01012, doi:10.1029/2008GC002234.

Campillo, M. & Paul, A., 2003. Long-range correlations in the diffuse seismic coda, *Science,* **299,** 547–549.

Cho, K.H., Herrmann, R.B., Ammon, C.J. & Lee, K., 2007. Imaging the upper crust of the Korean Peninsula by surface-wave tomography, *Bull. seism. Soc. Am.,* **97,** 198–207.

Dahlen, F.A. & Tromp, J., 1998. *Theoretical Global Seismology,* Princeton Univ. Press, Princeton, New Jersey.

de Hoop, M.V., Solna, K., 2008. Estimating a Green's function from field–field correlations in a random medium. *SIAM J. Appl. Math.,* **69**(4), 909–932.

Harmon, N., Forsyth, D. & Webb, S., 2007. Using ambient noise to determine short-period phase velocities and shallow shear velocities in young oceanic lithosphere, *Bull. seism. Soc. Am.,* **97,** 2009–2023.

Harmon, N., Gerstoft, P., Rychert, C.A., Abers, G.A., Salas de la Cruz, M. & Fischer, K.M., 2008. Phase velocities from seismic noise using beamforming and cross correlation in Costa Rica and Nicaragua, *Geophys. Res. Lett.,* **35,** L19303, doi:10.1029/2008GL035387.

Kang, T.S. & Shin, J.S., 2006. Surface-wave tomography from ambient seismic noise of accelerograph networks in southern Korea, *Geophys. Res. Lett.,* **33,** L17303.

Liang, C. & Langston, C.A., 2008. Ambient seismic noise tomography and structure of east North America, *J. geophys.Res.,* **113**(B3), B03309, doi:10.1029/2007JB005350.

Lin, F.-C., Ritzwoller, M.H., Townend, J., Bannister, S. & Savage, M.K., 2007. Ambient noise Rayleigh wave tomography of New Zealand, *Geophys. J. Int.,* **170**(2), 649–666, doi:10.1111/j.1365–246X.2007.03414.x.

Lin, F.-C., Moschetti, M.P. & Ritzwoller, M.H., 2008. Surface wave tomography of the western United States from ambient seismic noise: Rayleigh and Love wave phase velocity maps, *Geophys. J. Int.,* **173**(1), 281–298, doi:10.1111/j1365–246X.2008.03720.x.

Lobkis, O.I. & Weaver, R.L., 2001. On the emergence of the Green's function in the correlations of a diffusive field, *J. acoust. Soc. Am.,* **110,** 3011–3017.

Malcolm, A.E., Scales, J.A. & van Tiggelen, B.A., 2004. Extracting the Green's function from diffuse, equipartitioned waves, *Phys. Rev. E,* **70,** 015601.

Montagner, J.-P., 1986. Regional three-dimensional structures using long-period surface waves. *Ann. Geophys.,* **4,** 283–294.

Moschetti, M.P., Ritzwoller, M.H. & Shapiro, N.M., 2007. Surface wave tomography of western United States from ambient seismic noise: Rayleigh wave group velocity maps, *Geochem., Geophys., Geosys.,* **8,** Q080101, doi:10.1029/2007GC001655.

Nakahara, H., 2006. A systematic study of theoretical relations between spatial correlation and Green's function in one-, two- and three-dimensional random scalar wavefields, *Geophys. J. Int.,* **167,** 1097–1105.

Prieto, G.A. & Beroza, G.C., 2008. Earthquake ground motion prediction using the ambient seismic field, *Geophys. Res. Lett.,* **35,** L14304, doi:10.1029/2008GL034428.

Prieto, G.A., Lawrence, J.F. & Beroza, G.C., 2009. Anelastic Earth structure from the coherence of the ambient seismic field, *J. geophys. Res.,* **114,** B07303, doi:10.1029/2008JB006067.

Rhie, J. & Romanowicz, B., 2006. A study of the relation between ocean storms and the Earth's hum, *Geochem. Geophys. Geosyst.,* **7**(10), doi:10.1029/2006GC001274.

Roux, P., Sabra, K.G., Kuperman, W.A. & Roux, A., 2005. Ambient noise cross correlation in free space: theoretical approach, 2005, *J. acoust. Soc. Am.,* **117,** 79–84.

Sabra, K.G., Gerstoft, P., Roux, P. & Kuperman, W.A., 2005. Surface wave tomography from microseisms in Southern California, *Geophys. Res. Lett.,* **32,** L14311, doi:10.1029/2005GL023155.

Shapiro, N.M. & Campillo, M., 2004. Emergence of broadband Rayleigh waves from correlations of the ambient seismic noise, *Geophys. Res. Lett,* **31,** L07614, doi:10.1029/2004GL019491.

Shapiro, N.M., Campillo, M., Stehly, L. & Ritzwoller, M.H., 2005. High-resolution surface wave tomography from ambient seismic noise, *Science,* **307,** 1615–1618.

Simons, F.J., Van Der Hilst, R.D., Montagner, J.-P. & Zielhuis, A., 2002. Multimode Rayleigh wave inversion for heterogeneity and azimuthal anisotropy of the Australian upper mantle, *Geophys. J. Int.,* **151,** 738–755.

Smith, M.L. & Dahlen, F.A., 1973. Azimuthal dependence of Love and Rayleigh-wave propagation in a slightly anisotropic medium, *J. geophys. Res.,* **78,** 3321–3333.

Snieder, R., 2004. Extracting the Green's function from the correlation of coda waves: a derivation based on stationary phase, *Phys. Rev. E,* **69,** 046610, doi:10.1103/PhysRevE.69.046610.

Stehly, L., Campillo, M. & Shapiro, N.M., 2006. A study of the seismic noise from its long range correlation properties, *J. geophys. Res.,* **111,** B10306, doi:10.1029/ 2005JB00237.

Tsai, V.C., 2009. On establishing the accuracy of noise tomography travel-time measurements in a realistic medium, *Geophys. J. Int.,* **178**(3), 1555–1564, doi:10.1111/j.1365-246X.2009.04239.x.

Wapenaar, K., 2004. Retrieving the elastodynamic Green's function of an arbitrary inhomogeneous medium by cross correlation, *Phys. Rev. Lett.,* **93,** 254301.

Wapenaar, K., Slob, E. & Snieder, R., 2006. Unified Green's function retrieval by cross correlation, *Phys. Rev. Lett.,* **97,** doi:10.1103/PhysRevLett.97.234301.

Weaver, R.L. & Lobkis, O.I., 2004. Diffuse fields in open systems and the emergence of the Green's function, *J. acoust. Soc. Am.,* **116,** 2731–2734.

Yang, Y. & Ritzwoller, M.H., 2008a. Characteristics of ambient seismic noise as a source for surface wave tomography, *Geochem. Geophys. Geosyst.,* **9,** doi:10.1029/2007GC001814.

Yang, Y. & Ritzwoller, M.H., 2008b. Teleseismic surface wave tomography in the western US using the Transportable Array component of USArray, *Geophys. Res. Lett.,* **35,** L04308.

Yang, Y., Ritzwoller, M.H., Levshin, A.L. & Shapiro, N.M., 2007. Ambient noise Rayleigh wave tomography across Europe, *Geophys. J. Int.,* **168,** 259–274.

Yang, Y., Li, A. & Ritzwoller, M.H., 2008. Crustal and uppermost mantle structure in southern Africa revealed from ambient noise and teleseismic tomography, *Geophys. J. Int.,* **174,** 235–248, doi:10.1111/j.1365–246X.2008.03779.x.

Yao, H., Van Der Hilst, R.D. & de Hoop, M.V., 2006. Surface-wave array tomography in SE Tibet from ambient seismic noise and two-station analysis—I. Phase velocity maps, *Geophys. J. Int.,* **166,** 732–744.

Yao, H., Beghein, C. & Van Der Hilst, R.D., 2008. Surface wave array tomography in SE Tibet from ambient seismic noise and two-station analysis—II. Crustal and upper-mantle structure, *Geophys. J. Int.,* **173,** 205–219.

Yao, H., Campman, X., de Hoop, M.V. & Van Der Hilst, R.D., 2009. Estimation of surface-wave Green's function from correlations of direct waves, coda waves, and ambient noise in SE Tibet, *Phys. Earth planet. Inter.,* doi:10.1016/j.pepi.2009.07.002.

Zheng, S., Sun, X., Song, X., Yang, Y. & Ritzwoller, M.H., 2008. Surface wave tomography of China from ambient seismic noise correlation, *Geochem. Geophys. Geosyst.,* **9,** Q0502, doi:10.1029/2008GC001981.